PROCEEDINGS
OF THE EVENT
IPSP2017
INDUSTRIAL
PROBLEM SOLVING
WITH PHYSICS

Trento (Italy)
July 17 – 22, 2017
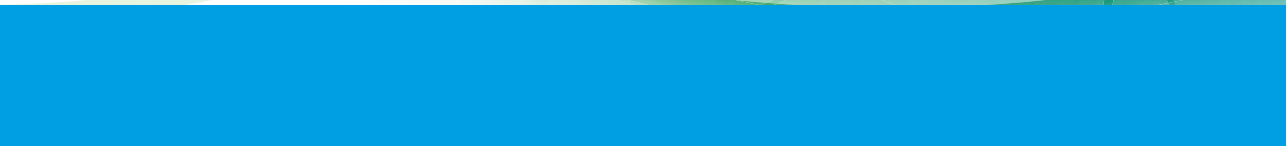
Proceedings of the event IPSP2017

Industrial Problem Solving with Physics
Trento, July 17th – 22nd, 2017

Editors

Carmelo Mordini
Marco Zanoli

Scientific Committee of Industrial Problem Solving with Physics 2017

PREFACE

Confindustria Trento is partner of IPSP since the very first edition. When the founders of the competition – three PhD students of the Physics Department of UNITN – presented us their idea, we decided to join the project mainly for three reasons. First of all, it is a bottom-up initiative, managed by proactive students. Moreover, it contributes to promote the role of graduates and PhDs in Physics within the industrial sector. Finally, it can really help to narrow the gap between research and industry.

So far, our experience with IPSP has been extremely positive. Companies who participated in IPSP have obtained innovative solutions to their technical problems, with important effects on their products and productive processes. That is why we will support IPSP in the future too. Let's innovate together!

Alessandro Santini, Confindustria Trento

IPSP, at its 4th edition, confirms itself as a unique opportunity for sharing know-how and growth experiences for young physicists, researchers and companies, allowing young talents to test the skills they acquired through their academic training together with their scientific creativity. At the same time, companies will be able to find innovative solutions and alternative paths to achieve their goals, proposed by people who stay outside their "day-by-day" activity.

From the same perspective, Trentino Sviluppo has always been promoting the connection between research and business. This is exactly what happens in Polo Meccatronica, a shared technological park where companies, students and researchers interact to face the new challenges of Industry 4.0. The same "knowledge triangle" is the basis of the ProM Facility project, the innovative 4.0 laboratory of Polo Meccatronica that allows companies, students and researchers to get to know and learn to use the new technologies related to prototyping and additive manufacturing. Recognizing the importance of the circular transfer of knowledge, Trentino Sviluppo confirms its commitment to involve companies based in Polo Meccatronica to participate in IPSP and benefit from the fresh mind and the ability to think "outside the box" of Physics students.

Paolo Gregori, Polo Meccatronica

Industrial Problem Solving with Physics has reached in 2017 its 4th edition and from a Technology Transfer perspective it keeps consolidating a new model of industry-academia collaboration, which allows industrial problems to be solved quickly and effectively in one week. A growing trend within the initiative consists in a series of meetings between the university and the enterprises involved in IPSP after the event, fostering long term collaborations encouraged by the contribution of Trentino Sviluppo – Polo Meccatronica and Confindustria Trento. Indeed, one of the main targets of IPSP is the development of a strong link between university laboratories and enterprises. Both applied research and placement of young scientist can profit from the dialogue promoted by this event.

Vanessa Ravagni, Research Support and Technology Transfer Division,
University of Trento

INTRODUCTION

IPSP – Industrial Problem Solving with Physics is an event organized by the Department of Physics, the Doctorate School in Physics and the Research Support and Knowledge Transfer Division of the University of Trento, in collaboration with Confindustria Trento and Trentino Sviluppo – Polo Meccatronica. After four years of activity, it is now established as one of the most peculiar and innovative initiatives of the Physics Department.

The event was born from an idea of PhD students with a precise aim: to promote the physicist's role as a contact point between the industrial world, facing everyday new technological challenges, and the academia, that is the place where young researchers naturally develop both the attitude to investigate and the skills to solve those problems.

The format is simple yet effective: the companies are asked to propose one or more problems regarding their industrial processes, their production or the technologies involved in that. For each of the selected problems a team of "brains" formed by master students, PhD students and research fellows will work for one week trying to find a suitable solution. In this short time both the students and the companies experience a new way of putting their knowledge at work together, a teamwork experience which has revealed to be the real engine of our initiative. The success of the event among the companies proved the value of the contribution given by the students to the R&D process, and has naturally strengthened the relationships between the Physics Department and the involved industries with the opening of research opportunities, scholarships and collaborations.

Following the positive trend of past years, IPSP2017 has seen a strong motivation in both sides of its participants. We received applications from 11 companies, with a total number of 19 proposed problems, and three out of them were selected and proposed to our 25 brains. The catchment area of the event continued to grow, since on one hand some of the interested companies were located outside the Trento area, and on the other hand we had five students coming from other universities, who were hosted for the whole duration of the event.

The brains worked hard and concluded the week presenting valuable solutions to their respective problems. This volume reports a scientific and technical description of the activities carried out by the three teams of IPSP2017. Each chapter begins with a brief presentation of the company and a description of the proposed problem, followed by a review of the different paths the team explored in search for the solution and a report on the proposed final results.

Carmelo Mordini, Marco Zanoli
Scientific Committee of IPSP2017
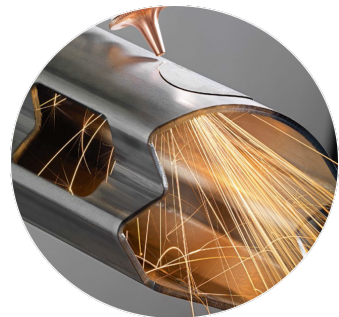
ANALYSIS OF THE LASER PIERCING PROCESS

F. Getman, M. Marcante, A. Mezzadrelli, C. Mordini, L. Parisi, Y. Popat, M. Previde Massara, M. Rossignoli, S. Signorini

1.1 Introduction

1.1.1 The company

BLM GROUP (BLM Spa, ADIGE Spa and ADIGE-SYS Spa) is a worldwide leader company in the fields of laser cutting, bending, saw cutting and end-forming of metallic tubes.

In particular, ADIGE Spa is specialized in the production of laser cutting systems and machines for the cutting of tubes [1]. The company has developed several types of laser tube-cutting machines with different application fields depending on the metal piece shape and dimension (metal sheet or tube with diameters ranging from 12 to 610 mm), on the type of cutting (2D or 3D) or the type of laser (fiber laser or CO_2 laser) [2].

1.1.2 The piercing-cutting process

The cutting process is performed in two steps:

1. the piercing process;

2. the cutting process.

The laser piercing process involves a pulsed wave regime of operation, which allows a better heat control and the creation of a hole from which it is possible to perform the cutting process with a continuous wave regime of operation.
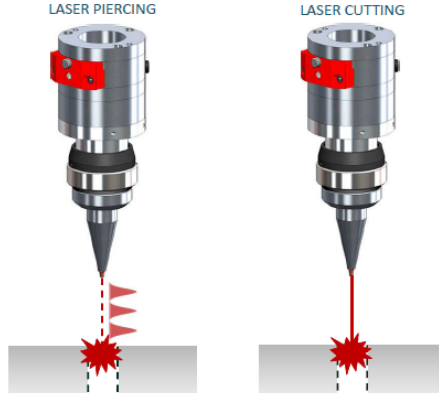
1

Figure 1.1: (Left) Laser piercing process with a pulsed-laser permits to drill the target. (Right) The continuous wave laser allows to perform the complete cutting of the metal piece.

The laser-cutting machine presented by BLM Adige group is characterized by an optical system composed by lenses, collimators and mirrors, that focuses the optical beam of a fiber laser on the sample. The ending part of the cutting system is characterized by a flux of gas, which exits from the cutting system and that is directed towards the sample, following the same path of the optical beam. The gas flux is used for two reasons:

- to ease the heat conduction;

- to blow away the fused metal inside the hole.

1.1.3   The problem

The problem presented by Adige and studied during IPSP 2017 concerns the piercing process of a steel sample (structural steel S355 EN10025:2004). The first laser pulses that reach the sample may exhibit unwanted phenomena, with detrimental effects for the cutting process and the final quality of the cut metal piece. In particular, these initial

Figure 1.2: Sketch of the laser-cutting machine.

pulses lead to the ejection of droplets of molten material from the sample. These droplets can reach the inner optics of the laser machine, damaging the protection window, depicted in in Fig. 1.2: this results in a waste of money and time, since the laser-machine has to be periodically stopped in order to substitute this protection glass. Another problem is that the ejected material solidify just outside the hole, resulting in a lower quality of the cutting process.
The solution to be investigated should minimize both the amount of the recasted
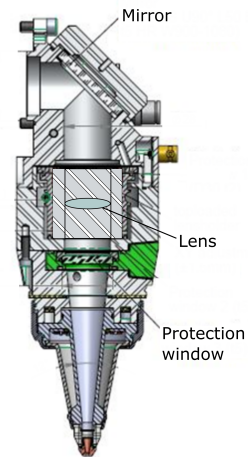
material on the metal piece and the metal droplets reaching the lens of the cutting machine. Within this framework, the main request of the company was to provide them with a tool able to analyze the high speed videos (HSVs) of the piercing process, finding the main parameters that rule the recasted material formation and the droplets ejection. According to this idea, the company provided us with several HSVs of the process.

1.2 Approach to the problem

The approach adopted in the week to face up the problem was first of all to look at the HSVs already performed by the company, in order to identify the peculiar features ruling the process (such as the maximum height of the drops, their velocity and the area of the recasted material), and then to develop a video-analysis software able to measure these features. We also planned new HSV measurements to understand the role of the working parameters of the laser-machine on the piercing process. Regarding the role of the working parameters, we also performed scanning electron microscopy (SEM) and microscope measurements in order to look at the recasted material distribution. Moreover, a simplified theoretical analysis was conducted with a ballistic approach.

The final goal was to find the correlation between the working parameters of the machine and the above mentioned features characterizing the process; the knowledge of this correlation can be used to optimize the piercing process by changing the input parameters of the machine.

1.2.1 High speed videos and set-up

The small dimension of the elements involved and the huge speed of the process require the use of a high speed camera with a resolution sufficient to identify the metal droplets. The company provided us with the high speed camera Photron Fastcam Mini AX200, whose acquisition performance can vary from 6400 fps (1024 × 1024 pixels, horizontal × vertical) to 900000 fps (128 × 16 pixels). The camera was mounted as in Fig. 1.3, where the set-up used for the measurements is shown. The camera was tilted by an angle θ with respect to the horizontal plane. A 640 nm laser light source was used to illuminate the scene.

The piercing process had to be characterized as a function of the different working parameters of the laser machine. The machine and the working parameters that could be changed are shown in Fig. 1.4.

The company provided more than 20 different videos of the piercing process with their laser machine. The videos were obtained with a resolution of 384 × 256 pixels at 50000 fps, with an inclination of the camera of 30 degrees. By observing the HSVs, first of all we identified the three main steps characterizing the piercing process, also reported in Fig. 1.5:

- "Ghost" formation at the first laser impulse;

- metallic fountain of fused material that exits from the hole;
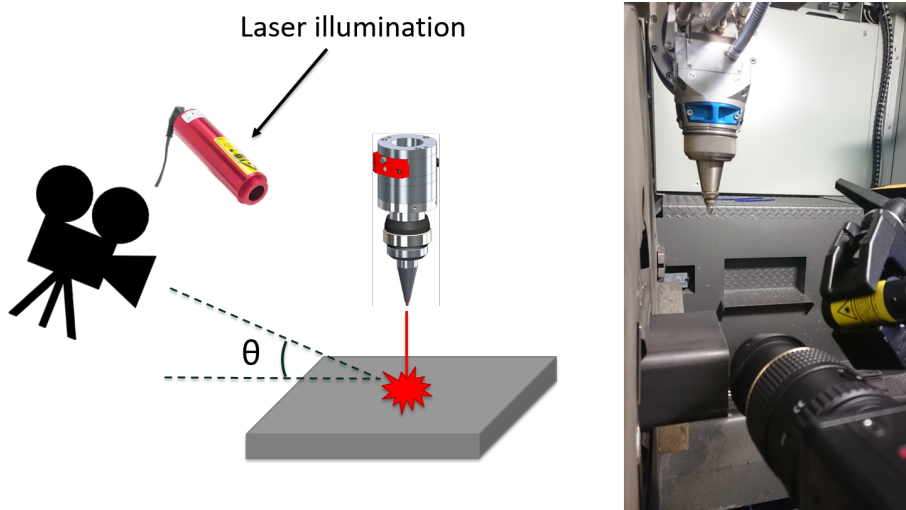
Figure 1.3: (Left) Sketch of the set-up used for the acquisition of the HSVs. The camera was tilted by an angle θ with respect to the horizontal plane. A laser light source was used to illuminate the scene. (Right) Picture of the real set-up.

Figure 1.4: Laser machine with the detail of the nozzle. The parameters that could be changed were: the gas flow pressure, the laser power and pulse duration, the beam focus and the stand off distance (SOD).

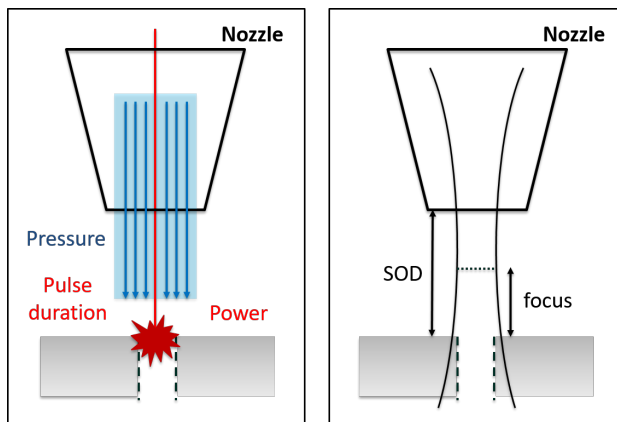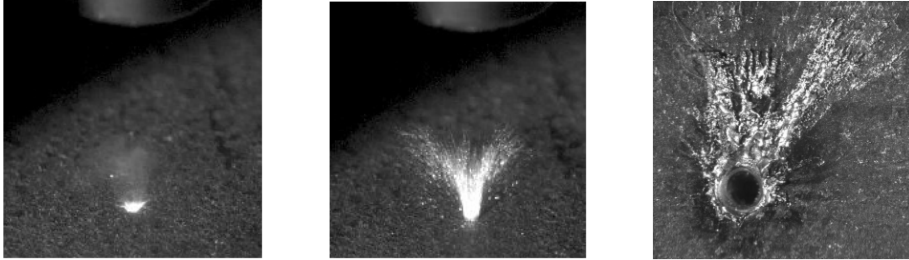- recasted material around the hole when the process has finished.

Figure 1.5: (Left) "Ghost" formation. (Middle) Metallic fountain. (Right) Recasted material around the hole.

Through the videos we understood the main features governing the quality of the process, that will be called "output parameters" in the following, shown in Fig. 1.6:

- the maximum height reached by the molten material;

- the amount of recasted material in the area around the hole;

- the diameter of the hole fabricated.

1.2.2 Finding the best parameters

In this section we describe the method we used in order to find the best input parameters for the piercing process. We considered the two problems pointed out by the company: the damage of the apparatus lens and the accumulation of recasted material around the hole.

Inspecting the videos provided by the company, we carried out an analysis in order to determine which input parameters are mainly related to the two problems. From the analysis we were able to give an experimental plan to the company in order to probe different combinations of the input parameters. Finally, we wrote a Python software in order to analyze the videos in a more efficient and rigorous

Figure 1.6: (a) Height of the fountain. (b) Recasted material area around the hole. (c) Diameter of the hole.

way and to describe quantitatively the output parameters that matter in order to find a solution to the proposed problems.

Eventually, we were able to determine which input parameters most influenced the piercing process and which output parameters are most important to be observed in order to control the piercing process. In this way, we found a particular combination of best parameters in order to optimize the process.

Video analysis

In order to determine the best parameters for an efficient piercing process, we started by looking at the videos the company provided us. We divided the videos in six groups, with only one input parameter varying for each group. In this way we were able to determine if an effect was correlated to the variation of a particular parameter. The six input parameters we considered were: laser power, frequency and duty cycle, focus position, stand-off distance (SOD) and air flow pressure. What we observed, as shown in Fig. 1.7, is that by increasing the laser power, the height of the fountain increased, whereas both the recast material and hole diameter decreased. For smaller relative focuses we observed an opposite trend, that is the height of the fountain decreased, whereas the amount of recast material and the hole diameter increased. This last trend was observed also for the SOD. Finally, by increasing the fluid pressure, a smaller fountain and a larger amount of recast material were observed. There was no variation in the hole diameter due to pressure variations. Moreover, no particular trend was associated to the variation of the laser frequency and duty cycle.

So, we can conclude that the input parameters that are most responsible for some variations in the piercing process are the laser power, the nozzle relative focus, the SOD and the fluid pressure. Moreover, the most important output parameters to look at in order to have a high efficiency piercing process are the fountain height, the amount of recasted material and the hole diameter.

In order to analyze quantitatively the output parameters from the videos we wrote a Python code able to extract the investigated quantities from the HSVs. The parameters we extracted from the videos through the code were the maximum height of the molten material fountain with respect to the material surface, the area of the recasted material around the hole and the initial velocity of the particles forming the fountain. This last parameter could give information on the spread of the recast material around the hole. The code will be described in detail in section 1.2.3.

Experimental plan

In order to understand the statistics of the process, we planned the new HSV measurements according to the most important input parameters that we pointed out from the first observation of the videos.

In Fig. 1.8 the experimental plan to be carried out at Adige is shown. We performed 29 measurements. We varied the SOD in the range 3 - 7 mm, having the majority of the measurements at a SOD of 5 mm (the previous videos indicated that this was the best distance for our two problems). We then varied the

Parameter	Height	Recast	Hole diameter
Power ↑	↑	↓	↓
Focus ↓	↓	↑	↑
SoD ↑	↓	↑	↑
Pressure ↑	↓	↑	——

Figure 1.7: Effect of the input parameters on the height of the material fountain, recast material around the hole, hole diameter. The correlations were extrapolated from the videos the company provided us.

Number	Distance	Relative Focus	Focus	Pressure	Power	Frequency	Duty Cycle	Thickness
	mm	mm	mm	bar	kW	Hz	%	mm
1	5	0	5	12	3	500	50	5
2	5	-1	6	12	3	500	50	5
3	5	-2	7	12	3	500	50	5
4	5	-3	8	12	3	500	50	5
5	5	-4	9	12	3	500	50	5
6	5	-5	10	12	3	500	50	5
7	5	-1	6	12	2.5	500	50	5
8	5	-1	6	12	3	500	50	5
9	5	-1	6	12	3.5	500	50	5
10	5	-1	6	12	4	500	50	5
11	5	-1	6	12	4.5	500	50	5
12	3	-1	4	12	3	500	50	5
13	7	-1	8	12	3	500	50	5
14	3	-1	4	16	3	500	50	5
15	5	-1	6	16	3	500	50	5
16	7	-1	8	16	3	500	50	5
17	5	1	4	12	3	500	50	5
18	5	0	5	1	3	500	50	5
19	5	-2.5	7.5	1	3	500	50	5
20	5	-2.5	7.5	5	3	500	50	5
21	5	0	5	8	4	500	50	5
22	3	0	3	12	3	500	50	5
23	7	0	7	12	3	500	50	5
24	5	-1	6	12	3	500	50	5
25	5	-1	6	12	3	500	50	5
26	3	-1	4	12	3	500	50	5
27	5	-1	6	10	3	500	50	5
28	5	-2	7	12	3	500	50	5
29	5	-4	9	12	3	500	50	5

Figure 1.8: List of the planned measurements done during the day spent in Adige. Colored boxes represent how we varied the parameters. Different colors stand for different parameters. Here Distance refers to SOD.

SAMPLE	num	14	16	19
Standoff distance	mm	5	3	5
Relative focus	mm	-1	-2,5	0
Pressure	bar	12	16	8
Power	kW	4	3	4
Frequency	Hz	500	500	500
Duty cycle	%	50	50	50
Thickness	mm	5	5	5

Our parameters   **Bad parameters**   **Company's parameters**

Figure 1.9: Values of the input parameters in three cases: our best evaluation, when there is a large amount of recast material, current values used by the company. It is clear from the figure that both in our and company's choices the amount of recast material is acceptable.

relative focus between 0 mm and −5 mm. Regarding the pressure, the most of the experiments were taken at 12 bar and 16 bar. We performed just 4 measurements at low pressure (8, 5, 1 bar), since in this case the fountain reaches the nozzle, damaging immediately the protection window. Finally, we varied the power between 2.5 kW and 4.5 kW having the majority of the measurements at a medium value of 3 kW.

Best parameters determination

By analyzing the videos through the Python software we were able to evaluate quantitatively the role of the parameters involved in the process, finding the best combination of input parameters to optimize both the height of the molten material fountain and the amount of recast material, as shown in Fig. 1.9. The best values are: SOD of 5 mm, relative focus of −1 mm, pressure of 12 bar, power of 4 kW. Frequency and duty cycle are kept at 500 Hz and 50% respectively. With respect to the set chosen by the company we changed two parameters: relative focus and pressure. We set a negative relative focus of the nozzle (−1 mm) in order to lower the height of the molten material fountain. Moreover, we increased the pressure from 8 to 12 bar in order to reduce the fountain height, still having a low quantity of recast material around the hole.

As it can be seen from the figure, with our combination of input parameters, the amount and shape of recast material is acceptable and similar to the one obtained by using the current input parameters chosen as the standard by the company. In fact, as shown in fig. 1.10, in the case of our input parameters the fountain height is much less than in the case of the current values used by the company. So, with the new set of parameters found by our analysis we can reduce the amount of particles reaching the nozzle and then the lens, improving
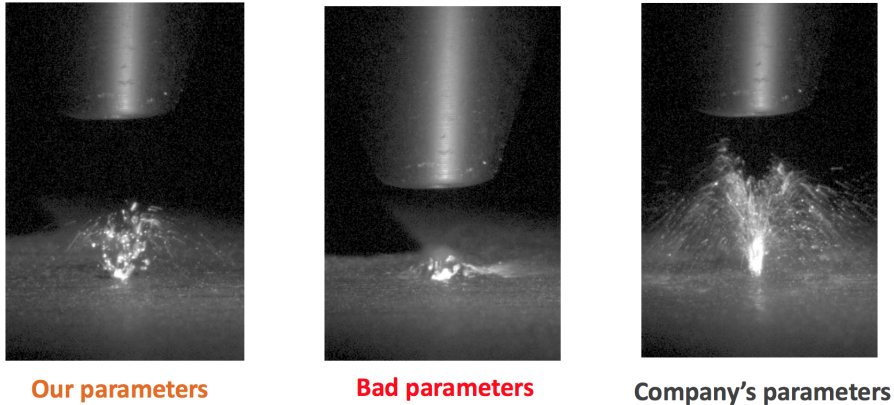
Figure 1.10: Picture of the ejected materials at their maximum height for the three configurations of Fig. 1.9. The fountain for the parameters we chose is very short with respect the corrent values used by the company, resulting in less material reaching the lens in the nozzle.

the piercing process.

In conclusion, we were able to find a new set of input parameters in order to optimize the output values of both the height of the molten material fountain and the amount of recast material around the hole. In this way, while preserving the quality of the hole, we reduced the number of particles reaching the lens, lowering its damaging.

1.2.3 The Software

We decided to develop a software able to analyze the videos acquired by the high speed camera. The main goal of the software is to estimate quantitatively from a video acquired by the high-speed camera some parameters able to characterize the recast material expulsion. To achieve sufficient statistical accuracy, one also requires to analyze a large number of videos, and manual inspection of each video becomes impractical and expensive. As such we need our software to automatize the analysis process in order to minimize the amount of human interaction needed per video. Unfortunately the class of possible sequences recorded is very large, with many different possible events. In fact, depending on the experimental configurations, events as diverse as ejection of a spray of molten liquids, formation of droplets, reboiling of the liquid inside the holes and many others (see Fig. 1.11) were observed. It is thus very difficult to write a simple algorithm able to distinguish among all these different events in a reliable way. We are also limited by the time resolution of the camera, as ejected particles often move on a timescale much faster than the interval between two successive frames, hindering the possibility to track particles among several frames. An additional difficulty consist in the impossibility of locating the precise position of the recast material in 3D space from a single point of view. This problem could be solved by cross-referencing several frames taken at the same time from different point of views,
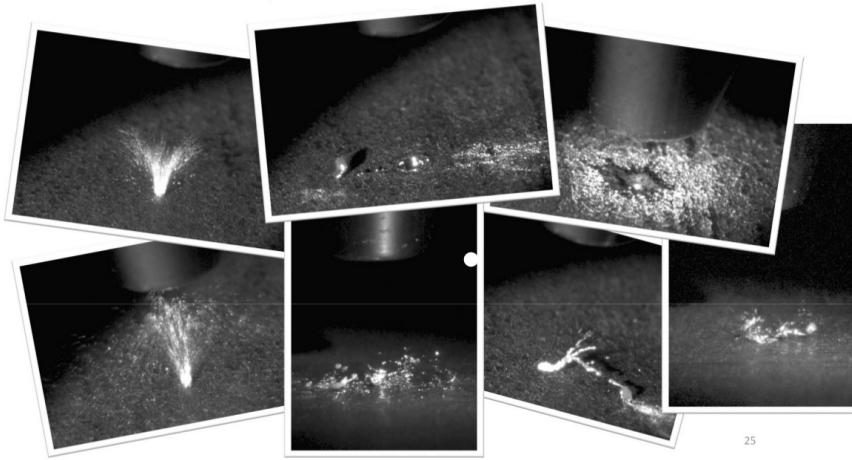
Figure 1.11: A few frames acquired by the camera with different experimental parameters.

but this is not possible partly as the company only owns one single high speed camera and partly because of constraints due to the geometry of the experimental setup. However the problem can be mitigated by a suitable orientation of the camera. Also, due to the high variability of the observed ejections, looking at individual particles of ejected material may not convey useful information in order to understand the physical process as a whole. Thus we follow the approach to focus on *global properties* and in particular to the two most important properties for the optimization of the process, the maximum height of the recast material and the amount of recast material close to the hole.

The Implementation

We implement the algorithm using the open source Python programming language, taking advantage of several packages freely available. The software is able to distinguish the recast material from the background and to subdivide it into clusters. This allows to take several kind of measurements.

- **Distribution**: it is possible to obtain the shape of the recast material on the 2D plane projected perpendicularly to the axis of the camera, at each time. The software is also able to recognize when the scattered material is broken in two different clusters, as shown in Fig. 1.12; Fig. 1.12a shows a frame of a sequence in which the material was ejected from the hole in the form of several big droplets in different directions,and Fig. 1.12b corresponds to the same frame but after the software analysis: the software is clearly able to correctly identify and discriminate different droplets.

- **Maximum height**: It is possible to obtain the maximum height of the recast material on the 2D image. This parameter is of crucial importance
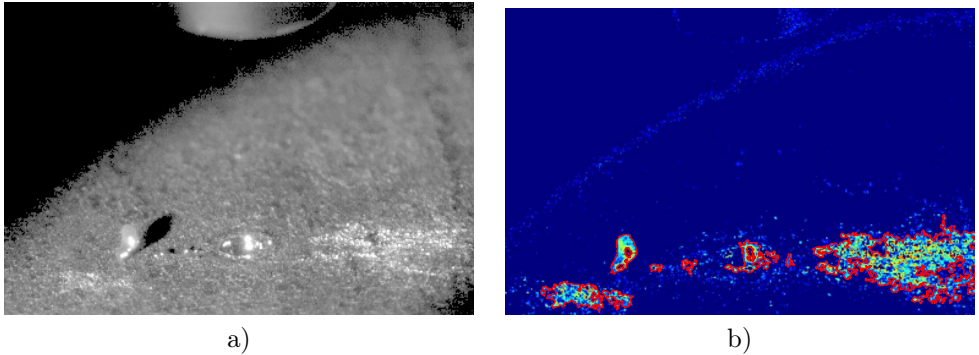
a)   b)

Figure 1.12: a) Frame acquired by the camera where the recast material takes the form of several big droplets . b) In the analyzed image we show that the software is able to recognize and distinguish different droplets.

to understand the likelihood of damage the lens. It is possible to get the maximum height of any kind of droplet.

- **Area**: The fraction of area in the frame covered by the recast material around the hole. This parameter is important to understand the quality of the cut. Unfortunately, it is not able to determine the thickness of the recast material.

- **Velocities**: Velocities can be measured from the distribution of the recast material in several frames. For instance it is possible to estimate the velocity at which the material is ejected from the hole during the piercing.

The algorithm

We now turn to a brief description of the algorithm used to analyze each frame.

- **Distinguishing recast material from the background**
  The images acquired typically are not very noisy and as neither the camera nor the sample move between a frame and another of the same video, the background remain fixed. It thus enough to subtract from each image the very first image, before any material is expelled, to distinguish the recast material from the background. To avoid mistaking a glare for recast material it is also necessary to impose a maximum cut off and discard any signal above this threshold. A minimum cutoff is also chosen to discard the noise from the camera. While the optimal values of these cut offs need to be specified from a human being, they mostly depend on the experimental setup and settings of the camera, and only weakly on the time evolution, and thus it is enough to only set them once per experiment.

- **Distribution of the scattered material** At this point we obtain the pixel positions of the scattered materials. As we are more interested on global properties, we want to measure the overall shape of the recast material. To
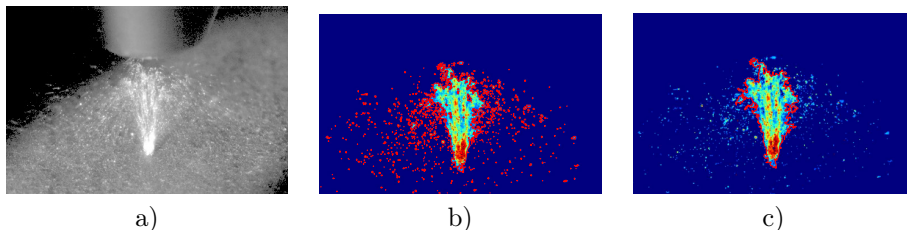
a)   b)   c)

Figure 1.13: a) Example of an image and two different analyzed images in false colors. b) and c) Analyzed images where the red line encloses respectively an high and moderate percentage of the total scattered material.

do this we compute closed contours of the ejected particles. We then merge all the contours which contain a certain percentage of the total scattered material in the image,taking into account possible overlaps. For high percentages we are able to divide the scattered material in all its constituent droplets, including very small and fast droplets. For lower percentages we are able to isolate the bulk of the scattered materials. In Fig. 1.13 we show the raw frame image next to two shapes of the the cloud obtained setting a low and high percentage. While in the first case we only select the bulk of the ejected material in the second we select all the tiny far-flung droplets of molten metal.

1.2.4   SEM and microscopy

In order to understand the size of the particles reaching the protection window, we performed scanning electron microscope (SEM) measurements of the nozzle and of the surface of the sample close to the piercing hole. The SEM was equipped with energy-dispersive spectroscopy analysis (EDS, INCA PentaFET-x3), in order to distinguish the materials during the SEM analysis. In Fig. 1.14 are shown two SEM images: one (Fig. 1.14a) taken close to the hole, showing that the diameter of the hole is around 300 μm; the other one (Fig. 1.14b) showing the particles reaching the nozzle during the piercing process, and it can be seen that the average size of these particles is around some microns.

In order to get insight on the distribution of recast material around the hole and to study its extent depending on the experimental conditions, also optical microscopy was performed. In Fig. 1.15a is shown the recasted material distribution when the hole is pierced with not optimal working conditions. In Fig. 1.15b the hole is pierced properly and no recasted material around the hole is present.

1.2.5   Theoretical modeling

In order to model the piercing process we would need to consider

- The distribution of energy from the laser beam inside the metal, and its phase transition from metal to plasma.

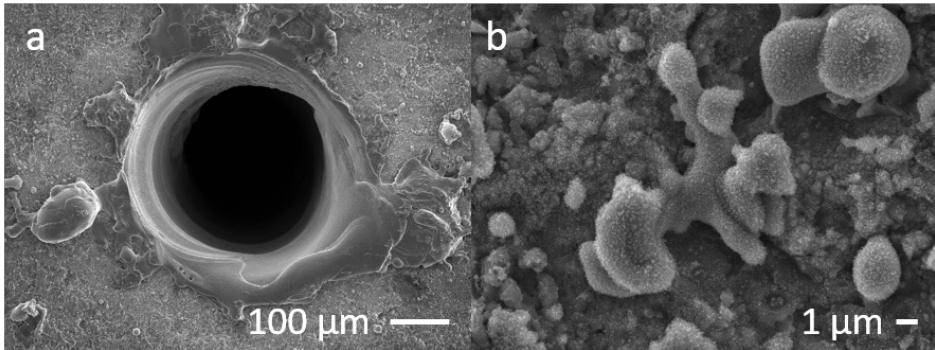- The explosion process caused by the rapidly vaporizing metal.

Figure 1.14: a) Pierced hole. b) SEM image of the nozzle border, where the particles ejected due to the piercing process are visible.
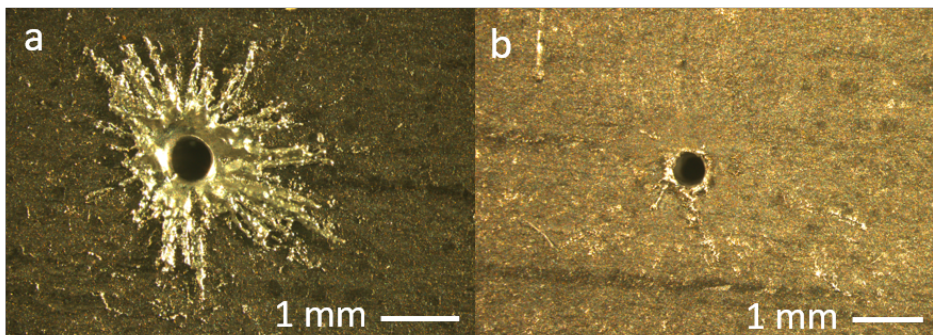

Figure 1.15: a) Hole with wrong input parameters, affected by a lot of recasted material around the pierced hole. b) Hole with good input parameter, with negligible recasted material.

- Fluidodynamics of the molten particles of the exploding metal inside a turbulent air flow.

All the above mentioned processes are very chaotic and the study of a single one of them would require more then the week that we had to solve the whole problem. For this reason we decided to approach a simplified version of only one of those three key processes, that is the fluid dynamics of the ejected particles inside the gas flow exiting from the nozzle. We decided to focus on this particular process since it is strictly related to one of the problems under study, that is the molten particles reaching the protection window. In particular, we want to model the efficiency of the gas flow in preventing the molten particles from reaching the nozzle.

In order to study this problem, we extracted the velocity of the ejected particles from the high speed videos. Hence, we concentrated our efforts on investigating the acceleration experienced by the particles when exposed to the gas flow. We studied only the worst case scenario, where the particles of the molten metal are ejected vertically from the pierced hole. To give a complete description of the process, we considered all the forces acting of the particles during their flight:

- **Air drag**: the force exerted by the fluid in motion with respect to the particle;

- **gravity**: the effect of the gravity on the particle;

- **radiation pressure**: the force exerted by the laser beam on the particle.

With the software, we measured an initial velocity of about 120 m/s for particles of radius around 20 microns; we expect the smaller particles to be faster, and the bigger particles slower.

The gravity was neglected, because its contribution to the deceleration is negligible, since in 5 mm, i.e. the SOD, this force can slow down the particles only by $\simeq 10^{-4}$ m/s.

We then considered the contribution of the laser radiation pressure as [3]

$$F_L = \frac{2}{c}\frac{P}{w^2\pi}r^2\pi \tag{1.1}$$

with c the light velocity, P the laser power, w the laser waist and r the radius of the molten particles. Regarding the force exerted by the gas flow on the particles, we calculated the drag force as [4]

$$F_D = \frac{1}{2}C_d\rho v^2\pi r^2 \tag{1.2}$$

with C_d the drag coefficient of a sphere, ρ the air density, v the relative velocity between the fluid and the particle. Since C_d is a function of the Reynolds number Re, we calculated Re as [5]

$$Re = v\rho r/\mu \tag{1.3}$$

where μ is the dynamic viscosity. In all our calculations we considered the dry air at 300 K as the fluid.
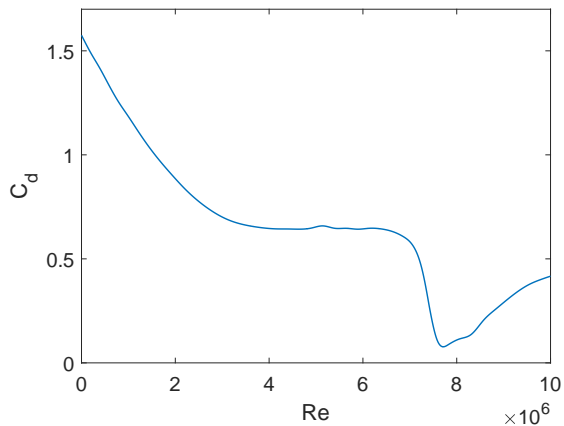
Figure 1.16: The drag coefficient on a the sphere in air flow for various values of the Reynolds number [5].

In order to calculate v, first of all we extracted from a simulation in literature [6], with the same experimental condition of our case, the pressure and velocity distribution of the gas flow as a function of the position between the nozzle and the metal surface, shown in Fig. 1.17. Then, we considered the measured lift-off velocity of the particles as constant along the path from the sample to the nozzle. This means that the resulting v is a conservative value.
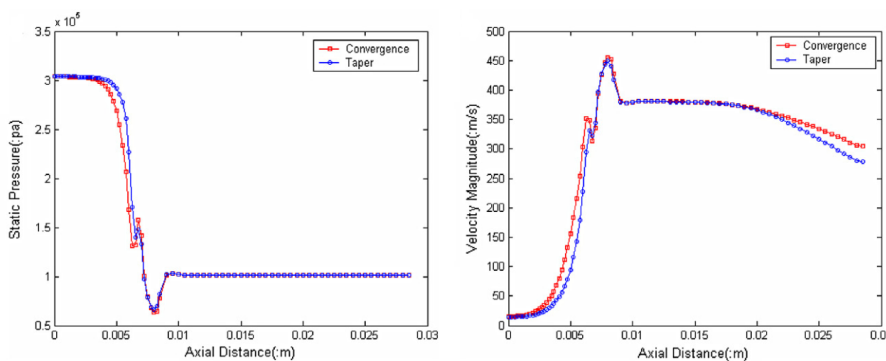

Figure 1.17: On the left, the distribution of the pressure outside the nozzle along the vertical axis. On the right, the distribution of the air velocity along the vertical axis [6]. The nozzle aperture is located at $0.008\ m$.

Considering the measured lift off velocity of 120 m/, with a SOD of 5 mm, the minimum average deceleration required to prevent the particles from reaching the nozzle is $a_{min} \simeq 4.32 \times 10^6 m/s^2$. This value is reported in Fig. 1.18, together with the decelerations provided by the drag and the radiation pressure. From this figure

we understand that also the radiation pressure is negligible with respect to the drag force. Moreover, we see that particles with $r \leq 3\mu m$ are stopped by the air flow. This result is compatible with the SEM measurements, which showed that only particles around some microns in size reach the nozzle. However, according to our model, also larger particles should be able to hit the nozzle, but they are not present experimentally on the nozzle surface. This may be due to the fact that we are not considering that larger particles have lower velocity. The model can be improved by studying the piercing process in more detail, evaluating also the velocity distribution of the particles as a function of the particle radius. This can be done by using the software that we implemented.
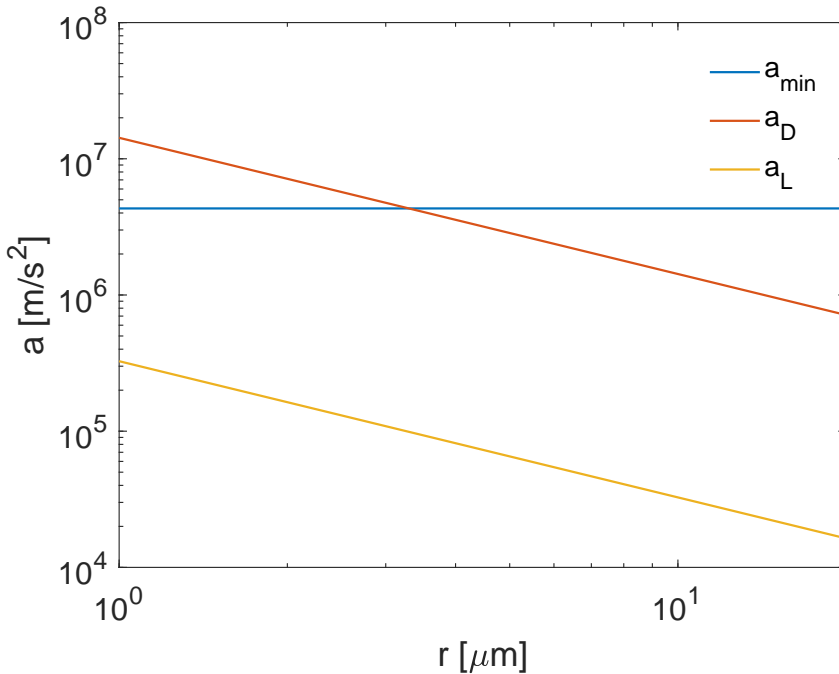

Figure 1.18: Accelerations involved in the process as a function of the particle radius. a_{min} is the minimum deceleration to apply to the particles to prevent them from reaching the nozzle. a_D is deceleration due to the drag force. a_L is the deceleration due to the radiation pressure.

1.3   Conclusions

During the week we faced the two problems given by the company: the lens damaging due to the piercing process and the recasted material deposition around the pierced hole. By solving these two problems the company could improve the quality of the cutting process, lowering at the same time the damage occurring at the last lens of the laser machine. The only tool available to approach the

problem was the HSVs of the piercing process. Actually, from the videos can be understood many significant features regarding the piercing process, that can be used to optimize its execution. Because of this, the company asked us to provide them with a tool able to analyze the HSVs, returning as the output the measurement of the most significant parameters of the process. Because of this, we studied the videos and the physics of the piercing in order to understand the crucial quantities governing the process, and then we developed a software able to measure these quantities from the HSVs. The software works, but it needs to be tuned better through the analysis of a larger amount of videos. We also studied in a very simplified manner the fluid dynamics of the molten particles when exposed to the gas flow exiting from the nozzle, finding results that are close to the experimental measurements. This means that the analytical model can give useful results in order to understand and optimize the piercing process, but it needs to be further improved, considering also the velocity distribution of the ejected particles as a function of their size.

The last step would be the application of the video analysis software, maybe together with a robust analytical model, to a more complete investigation of the process, with a suitable design of experiment, in order to characterize and optimize the piercing process.

Bibliography

[1] `http://www.ucimu.it/en/catalogue/companies/v/blm/`

[2] `http://www.blmgroup.com/en/lasertube`

[3] Wright, Jerome L. (1992), Space Sailing, Gordon and Breach Science Publishers

[4] Batchelor, G.K. (1967), An Introduction to Fluid Dynamics. Cambridge University Press

[5] https://www.grc.nasa.gov/www/k-12/airplane/dragsphere.html

[6] Hu, Jun, et al. Simulation and experiment on standoff distance affecting gas flow in laser cutting, Applied Mathematical Modelling 35.2 (2011): 895-902.

OIL HEATING PROCESS WITH MICROWAVES FOR COSMETICS

G. Abrusci, M. Barbiero, L. Basso, F. Bonaldo, P. Breviglieri, S. Malhotra, S. Merzi, S. Orioli, S. Tondini

2.1 Introduction

2.1.1 The company

Areaderma is a cosmetics laboratory founded 25 years ago and active in contract production of cosmetics and class I and IIA medical devices. Scientific research and innovation are at the foundation of their work.
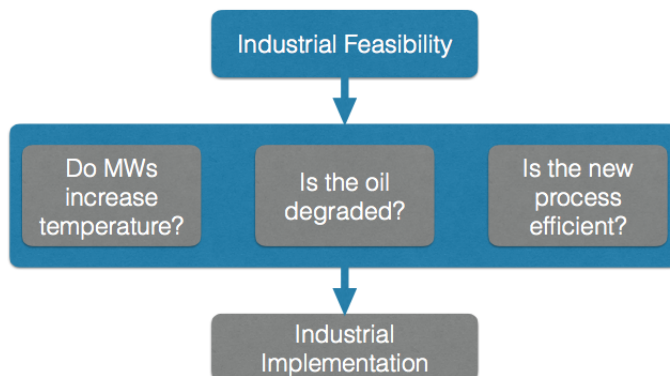
2.1.2 Statement of the problem

Figure 2.1: Schematic representation of the work flow followed during the week.

Cosmetic creams are generally composed by a mix of specific oils and water. In order to provide a cream, oils need to be mixed with water only when a specific temperature of the oils is reached, which is usually around 80° C [1]. This arises the key problem of heating the oils. In the Areaderma factory, oils are heated by putting them in containers surrounded by a water jacket, and the latter is heated by resistive heating. Although simple both conceptually and in its implementation, this process shows two main drawbacks:

- it is very slow, since it needs first to heat the water jacket and then to transfer the heat to the oil container (cfr. Section 2.4);

- it is power greedy, since the resistive heating is poorly efficient both in heating water and in the energy transfer (cfr. Section 2.4).

A natural question arises: whether a more efficient way of heating oils exists, and if such methodology could be in principle implemented in an industrial environment. In order to answer this, Areaderma proposed to our group to study what happens when the oils adopted in cosmetic applications are heated using microwaves. Indeed, microwaves should provide a more efficient way for heating the oils than the current technique, both in terms of time and energy, but to our knowledge no prior industrial application of this methodology has ever been implemented [1].

In order to answer Areaderma's question, during the week we followed the workflow presented in Fig. 2.1. First of all, we performed a generic feasibility study in order to understand if oils can be effectively heated by means of microwaves; this is reported in section 2.2. Since oil heating proved to be possible, we focused on the problem of understanding whether microwaves degrade oils during the heating process; our study is reported in section 2.3. Some oils showed to be more degradation-prone than others, but still the methodology seemed robust enough to study its efficiency and to compare it to the one of resistive heating; this is discussed in section 2.4. The efficiency gained by using microwaves instead of the typical water heating revealed to be so high that it convinced us that an industrial implementation of this process should be, as a matter of principle, possible. We investigated this possibility in section 2.5.

2.2 Assessment of feasibility

2.2.1 Microwave characterization

Microwave (MW) ovens represent nowadays a common device used to heat up food and water. Compared to conventional ovens used for cooking, the heating provided by microwave ovens is faster and more efficient. The physics behind the microwave heating process is fascinating and at the same time pretty simple, as explained by [2]. In MW oven, electromagnetic waves are created by a magnetron at 2.45 GHz and "guided" inside the microwave oven box by metallic waveguides. Waves, then, are reflected by the metal surfaces of the box and remain trapped inside the oven, heating the food (a more detailed discussion of the physics behind
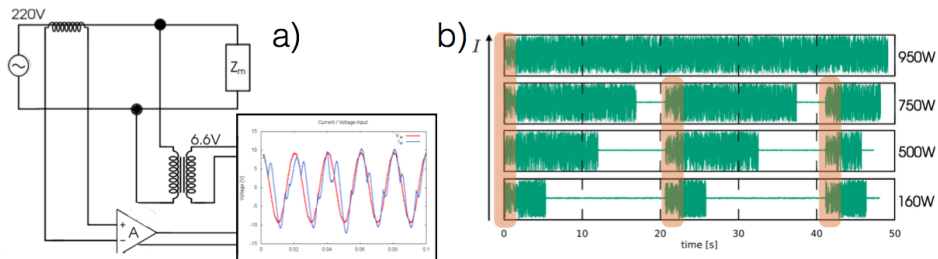
Figure 2.2: (a) Experimental apparatus used to probe the current and the voltage absorbed by MW oven (Z_m). The plot reports and example of dephasing between the current and the voltage. (b) Pwm cycle for different power settings. The pwm period is composed by an 'on' time, in which the magnetron is activated and power is delivered inside the cavity, and the 'off' time in which the magnetron is turned off. Different pwm power levels are obtained with different time sequences.

the heating mechanism is presented in section 2.2.3). In physics, a system in which waves travel back and forth with negligible energy losses is also called a *cavity*. The cavity is used to increase energy transfer rate between the electromagnetic waves and the system to be heated.

First of all, we were interested in how much electromagnetic energy is supplied by the MW oven and how this energy is delivered in time. In order to know the energy used by the system, we build a set-up to probe the current and the voltage absorbed by the MW oven in time. In Fig 2.2(a) we report the scheme we used to do so. The voltage absorbed by the MW oven was probed by a transformer that reduced the voltage from 220 V to 6 V. Instead, the current absorbed by MW oven was measured using and amperometric clamp and a voltage transducer (Tektronix AM503 current probe amplifier). First, the amperometric clamp and the voltage transducer are calibrated measuring the current flowing through a known resistor induced by a known voltage at 50 Hz, generated by a wave function generator (Agilent 34410A). Once the calibration is performed, the voltage and current signals are acquired using an oscilloscope (Agilent MSOX-2004A). With this probing experiment we discovered that:

- The phase difference between the voltage and the current is approximately $\phi \sim 8°$. This gives us an estimate of the power absorbed by the oven using the formula $P = I_{rms}V_{rms}\cos^2(\phi) \simeq 1.6$ KW. This values is in agreement with that of an independent measure performed with a Watt meter.

- The power transmission of the oven is regulated with a pulse-width modulation (pwm) technique. This is because it is not possible to vary the power output of the magnetron continuously, but it can only be turned off and on at a maximum. Switching its operation periodically regulates then the average power transferred to the cavity, which is proportional to the ratio of the 'on' time over the total period.
  The Fig 2.2(b) shows the power consumption of the oven in time at different power settings. The total pwm period is approximately 20 s, and at

each turn–on we observe a 1.2 s rising time, which is probably due to the magnetron switch on transient.
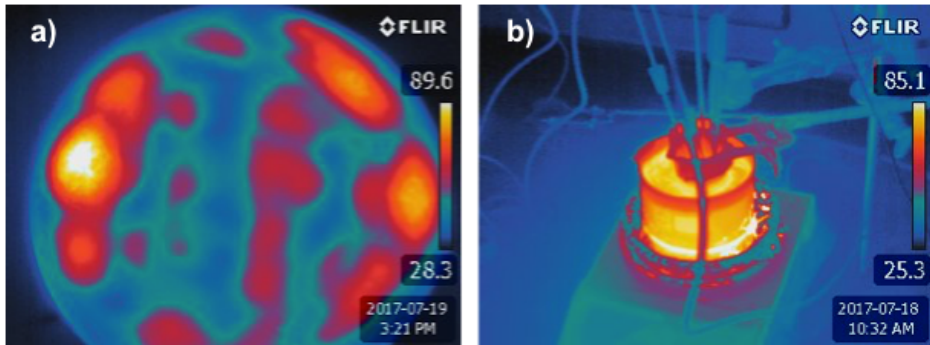
2.2.2   Hotspots

Figure 2.3: FLIR images of heated oil samples. (a) Temperature profile of an oil heated using microwaves. (b) Temperature profile of an oil heated using resistive heating.

In addition to standard thermometers, we used a FLIR infrared thermo-camera to measure the temperature variation of the oils. This allowed us to observe the spatial distribution of temperature and monitor the heat flow inside the oil during the heating process.

As a first measurement, the camera was used to take images before and after treating the sample with the two methods of microwave and resistive heating. The thermo-camera highlighted a key difference between the two: in the first case, Fig. 2.3(a), the oil shows a non trivial temperature profile, characterized by the presence of high temperature regions which we will call *hotspots*, while in the second case, Fig. 2.3(b), the oil is heated homogeneously. Overall, Fig.2.3(a) shows that MW oil heating is possible.

2.2.3   Dielectric Heating

MW ovens are commonly used to heat up foods, since they are composed by water in a noticeable quantity. Water molecules play a key role in the heating process with microwaves. Due to the absence of symmetry in their charge distribution, these molecules have an electric dipole that tends to align along the direction of an applied electric field. On the other hand, microwaves are electromagnetic waves, i.e. an oscillating electric and magnetic field. Therefore, in the presence of such field, water molecules experience a force due to this interaction that puts them in rotation. The frequency of the microwaves used in consumer ovens is chosen in order to maximize this effect. Since the molecules that absorb the MW are not in vacuum, their rotation is hindered by the interactions with the nearby molecules and part of the rotational energy is dissipated within the system as heat. [2]
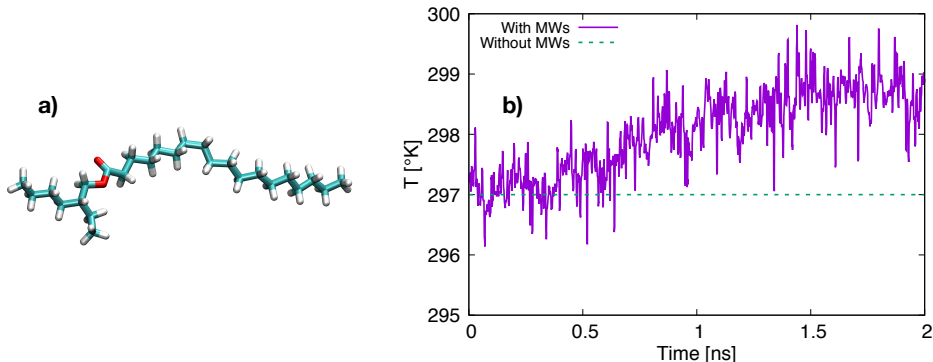
Figure 2.4: (a) Three-dimensional structure of the 2-ethylhexyl stearate. Carbon atoms are shown in cyan, while oxygen in red and hydrogen in white; (b) Average temperature of every 20 picoseconds with the oscillating electric field, compared with the average temperature of the same system in the NVT ensemble.

Does the same process apply to oil? In order to understand this we performed a molecular dynamics simulation of the most commonly used oil: 2-ethylhexyl stearate (2ES).

2.2.4 Molecular Dynamics Simulation

Since this oil is not used for biological simulations, we defined the set of parameters to compute the interactions during our simulation.

By means of the software VMD [3] and its plugins Molefacture and ForceField ToolKit, we built the three-dimensional structure of the 2-ethylhexyl stearate molecule, and the interaction constants by comparing its chemical formula [4] with the available parametrised lipids. As common in lipids, the carbon-hydrogen chain is highly flexible [4], therefore no constraints on the rigidity of these atoms were imposed.

The studied system consists of 1320 2ES molecules, arranged in a cubic lattice of side 100 Å to reproduce the experimental density of the oil. All MD simulations were performed using NAMD 2.12 [5] and the CHARMM36 force field [6].

Due to the high initial packing, the system was first minimized to remove steric clashes, and then heated up from 100 K to 300 K by 50 K every 1 ns in order to destroy the lattice order and reach a liquid phase. For the first three runs, the time step was set to 0.5 femtosecond. Afterwards, it was set to 2 fs: this allowed use to employ the SHAKE algorithm, fixing the bond between heavy atoms and hydrogen atom, and, hence, to speed up the computation. All simulations were performed with: periodic boundary conditions in all directions; a cutoff for short range non-bonded interaction of 12 Å; the particle mesh Ewald (PME) algorithm to include the contributions of long-range interactions. The ensemble sampled in the simulations was an isothermal-isobaric ensemble, at 1 atm, with a Nosé–Hoover Langevin barostat, with oscillation period 200 fs and decay coefficient 100 fs, and a Langevin thermostat, with damping coefficient 1 ps^{-1}. A simulation of 10 ns at
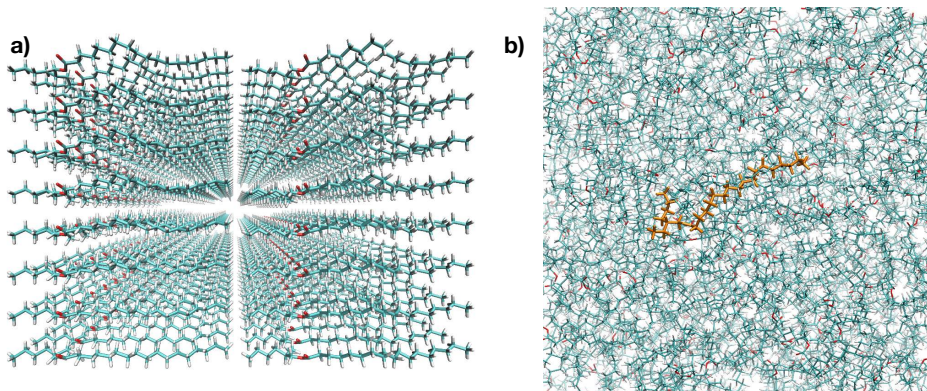
Figure 2.5: Setup of the simulation. (a) Part of the initial arrangement of 2-ethylhexyl stearate. (b) Equilibrated box. In orange a single molecule is highlighted for clarity.

300 K was performed to assess the equilibration of the system and and the first 5 ns were discarded in order to compute its equilibrium properties, such as the temperature.

To establish whether the oil could be heated by microwaves, i.e. an oscillating electric field, we simulated the system with an applied electric field along the x direction for 2 ns, due to the limited time at our disposal. We applied the electric field with a frequency of 5 GHz, higher than the working frequency of a consumer microwave oven but still in the micro-wave range, and an amplitude of 1 kcal/(mol Åe). Since in a microwave oven a stationary wave condition is reached, the field was allowed to vary every 5 ps to sample a cosine dependence, while the dimensions of the simulation box, much smaller than the microwave wavelength allowed us to *set* the system in an antinode of the standing wave.

Contrary to the previous cases, this time we simulated the box in a micro-canonical ensemble, i.e. we removed the thermostat effects, since it would have artificially subtract energy from the system and no increase in temperature would be possible to observe. Qualitatively, we observed an upward trend of the temperature if the electric field was applied. This effect cannot be taken into account within the fluctuations usually present in a simulation, while it should be ascribed to a form of energy transfer among rotating molecules, since the global translational velocity is removed before computing the temperature.

2.3 Oil Degradation

As it was already clear from Fig. 2.3, oils heated with microwaves do not show a homogeneous temperature profile. In particular, even if the mean temperature of the oil sample is around 80°C, microwave heating generates hotspots that can reach very high temperatures, in the order of 200°C [7]. This range of temperatures can bring to chemical degradation of the heated oils: for this reason, we performed some well-suited analyses on the microwave heated oils. We stud-

Bond type	Mean equilibrium length (Å)	Breaking length (Å)
C – C	1.55	2.30
C = O	1.22	1.83
C – O	1.33	1.99

Figure 2.6: Equilibrium distances among heavy atoms (data from CHARMM36 force field [6])

ied two different oils, typically used by the company as emollient: 2-ethylhexyl stearate and sunflower oil. The particular choice of the samples comes from the fact that they represent two of the most commonly used classes of oils in the cosmetic production. The first oil is a single molecule one, $C_{26}H_{52}O_2$, while the second one is a mixture of fatty acids, mostly oleic and linoleic acid. To check the potential chemical degradation upon microwave heating, first of all we simulated a box of 2-ethylexyl stearate at high temperature in order to see if any chemical bond breakage occurs and then we used three different spectroscopic techniques: Fourier-transform infrared (FT-IR) spectroscopy, performed in transmission mode at normal incidence using a JASCO FT-IR-660 plus spectrometer operated at room temperature; MicroRaman on a Jobin-Yvon Horiba LabRam Aramis equipped with a DPSS laser 532 nm; Nuclear Magnetic Resonance (NMR) spectroscopy with a Bruker Avance 400 NMR having a 9.4 T magnet.

2.3.1 High temperature MD simulation

In assessing the feasibility of the oil heating by means of microwaves, another pivotal point to be investigated was the oil degradation. This process involves changes in the chemical composition of the oil, in particular by the breaking of chemical bonds. Unfortunately, molecular dynamics simulations do not allow the modification of the system's chemical structure. A way to overcome this methodological limit is to observe the bond length. Due to the definition of bonds within the MD framework, they cannot break but they can stretch in an anomalous way, if an intense tensile stress is applied to the atoms forming a bond. Therefore, we simulated the equilibrated system at a temperature of 500 K, far beyond the temperature at which the oil is currently manipulated in the factory. After 1 ns of further equilibration, we analysed the bond-length distribution during another 2 ns of simulation. Except for the temperature, the other parameters of the setup were the same used in the previous run (see section 2.2.4). As a rule of thumb, if a bond exceeded its equilibrium length at room temperature by 150%, it was considered broken.

In table (2.6), the bond lengths among carbon and oxygen atoms are reported. Carbon atoms were parametrised differently according to their bonds with the nearby atoms, with an equilibrium distance between 1.53 and 1.56 Å. Most of the C–C bonds belonged to the latter category, hence, the reference distance in the table has been computed as a weighted average. No bonds between heavy atoms and hydrogen atoms were taken into account during the analysis, since the SHAKE algorithm was employed to constrain their length.

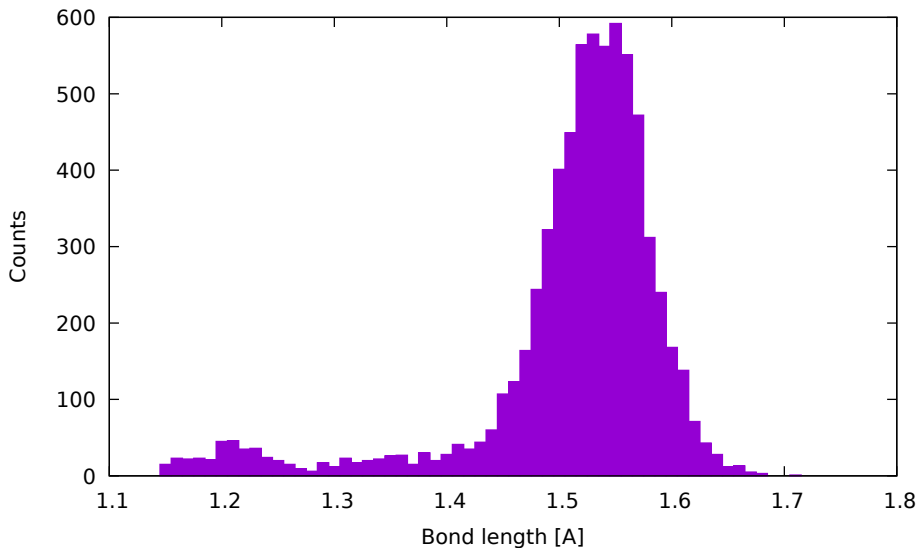As can been seen from figure 2.7, there is no evidence of *bond breaking*. In

Figure 2.7: Bond distribution. The highest peak is due to carbon-carbon bonds, which are the majority of the available bonds.

particular, bonds involving carbon atoms do not show any anomalous stretching, therefore, the energy in the system is not enough to produce any effects that can be related to the degradation of the oil. This result is in perfect agreement with the experimental measurements perfomed by our group.

2.3.2   Chemical Analysis: 2-Ethylhexyl Stearate

2-ethylhexyl stearate was heated to 85°C, both through water thermal bath and through microwave heating. Furthermore, a separate oil sample was heated up to ∼240°C directly with a hot plate. The oil was mixed by using a magnetic stirrer and the temperature was monitored with a PT100 thermocouple. The latter preparation was needed in order to understand what happens to a small sample which is brought to a temperature which is comparable to the one reached in the hotspots. We then compared the chemical properties of the heated oils with the ones of oil samples at room temperature (RT). The FT-IR and Raman spectra are shown in Fig. 2.8(a) and 2.8(b), respectively.

The two spectra present common features related to triglyceride functional groups [8]. The main features are:

- the peaks of C-H stretching symmetric (2850 cm^{-1}) and antisymmetric (2924 cm^{-1}) in -CH$_2$ and symmetric in -CH$_3$ (2897 cm^{-1});

- the peaks of C=O and C-O stretching at, respectively, 1770 cm^{-1} (stronger in FT-IR than Raman) and 1454 cm^{-1};

- the band of C-C stretching at 1150 cm^{-1};

- the peaks of C-H bending at 1463 cm^{-1} (scissoring) and 1302 cm^{-1} (twisting).

Obviously the two spectra present dissimilarities, due to the different sensitivity to different kind of vibrations, such as the peak at 2739 cm^{-1} in the Ramam spectrum, not present in the FT-IR spectrum, relative to C-H stretching of the -CH=O aldehyde group [9], or the region 700-1100 cm^{-1}, where different bands are present due to C-C stretching in different chains. The detailed interpretation of each peak is not of fundamental importance here, since we are mainly concerned about the eventual differences between the spectra of the heated and the room temperature oils. It is interesting to notice that neither the FT-IR nor the Raman spectra show any appreciable differences between heated and RT samples, meaning that microwave heating does not chemically degrade 2-ethylhexyl stearate. Neither the sample brought to 240°C shows any discrepancies with the RT sample, providing sign of a particular stable molecule. The larger signal of the black curve in the Raman spectrum Fig. 2.8 is due to a better focus of the laser beam onto the oil drop, and is not related to a different chemical composition.
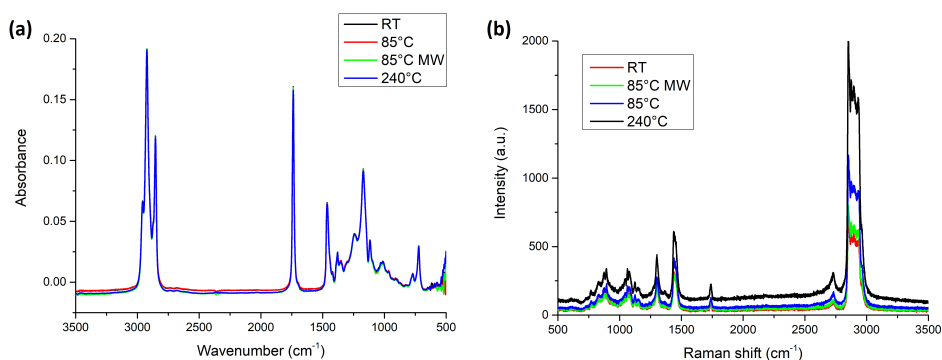

Figure 2.8: Spectroscopic analysis of 2-Ethylhexyl stearate. (a) FT-IR spectrum. Different curves refer to oil heated to different temperatures: oil at room temperature (black curve), heated to 85°C with thermal bath (red curve), to 85°C with microwave (green curve) and to 240°C (blue curve). (b) Raman spectrum. Comparison between non-heated oil (red curve), heated to 85°C with thermal bath (blue curve) to 85°C with microwave (green curve) and to 240°C (black curve).

2.3.3 Chemical Analysis: Sunflower Oil

We heated the multi-component oil, in our case the sunflower oil, following the same procedure described in section 2.3.2, with the only difference that the "hotspot sample" was brought to a temperature of about 295° C. The FT-IR spectrum of sunflower oil is given in Fig. 2.9(a), and it is almost identical to that of Fig. 2.8(a). Both the microwave heated samples (red curve) and the 295°C one are identical to the room temperature oil (black curve). More interesting in this case is the Raman spectrum, which is shown in Fig. 2.9(b). With respect to the spectrum of Fig. 2.8(b), Fig. 2.9(b) shows new peaks due to the presence
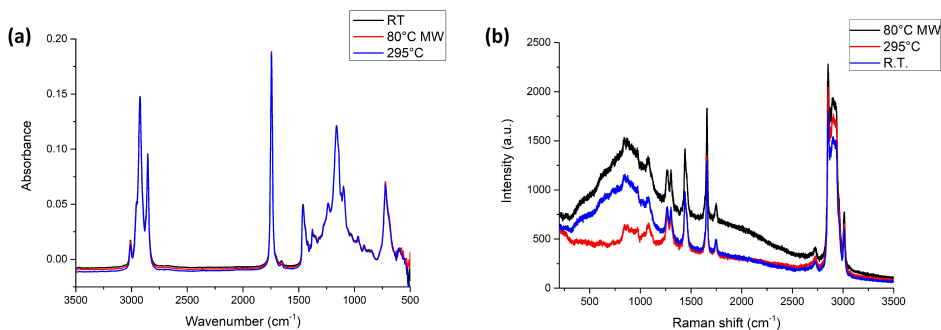
Figure 2.9: Spectroscopic analysis of sunflower oil. (a) FT-IR spectrum. Different curves refer to oil heated to different temperatures: oil at room temperature (black curve), heated to 85°C with microwave (red curve) and to 295°C (blue curve). (b) Raman spectrum. Comparison between non-heated oil (blue curve), heated to 85°C with microwave (black curve) and to 295°C (red curve).

of RRHC=CHR group and its internal vibration, such as the one at $3011\,\mathrm{cm}^{-1}$, attributed to the =C-H symmetric stretching, and the peak at 1658 cm^{-1}, related to the C=C stretching [10]. Moreover, the broad band at 500-1250 cm^{-1} is related to a convolution of peaks due to different C-C stretching in $-(CH_2)_n$- chains [10]. Most importantly, the sample homogeneously heated to 295°C shows an important difference in spectrum with respect to the other samples in the region 300-1000 cm^{-1}. This difference is likely related to the break of $-(CH_2)_n$- chains. The black curve relative to microwave heated oil shows the peaks superimposed to a broad band, which probably come from the glass substrate on which the oil drops are deposited, that is visible in this case due to a focus of the laser beam near the glass surface.

To confirm that chemical degradation of sunflower oil might occur at high temperature, we analyzed it with a more sensitive technique, which is the NMR
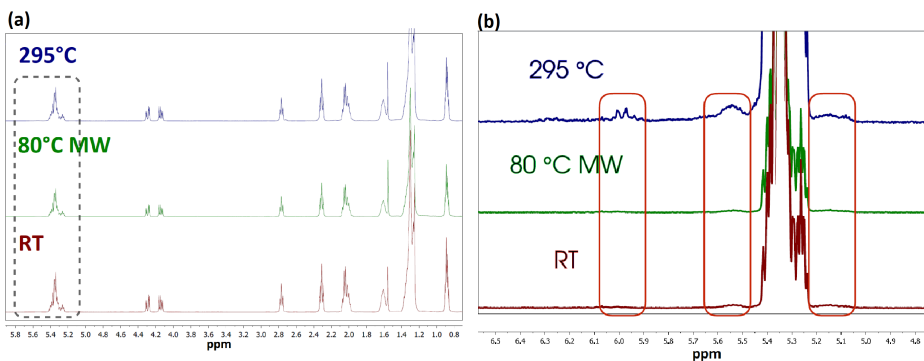

Figure 2.10: NMR analysis of sunflower oil. (a) Wide spectrum; (b) zoom of the dashed black box of (a): the red boxes indicates the region in which the different sample show differences.

spectroscopy. The NMR spectrum of the samples is given in Fig. 2.10(a), while 2.10(b) gives the same spectrum in a narrower chemical shift interval. The red boxes indicate additional peaks that arise in the 295°C sample, confirming chemical degradation of heated sunflower oil. Even though the signal of the high-temperature heated sample shows significant differences in the NMR spectrum with respect to the RT sample signal, the spectrum provided by the microwave heated sample looks identical to the RT one. This might indicate that, since hotspot regions generated via microwave heating are small and localized, they result in a small number of broken molecules which doesn't affect the overall chemical properties of the oil.

The take home message is that chemical degradation should be assessed for every oil used as precursors for cream preparation, and particular attention must be paid to multi-component oils, that can contain longer and less stable molecules. Moreover, in order to conceive a proper mixing of the oil, the position and the temperature of the hotspots inside the microwave oven need to be studied, allowing for a more homogeneous temperature profile. This point will be further discussed in section 2.5.

2.4 Process efficiency

After assessing the degradation properties of two different oils upon microwave heating, we performed quantitative measurements in controlled conditions in order to determine the efficiency of the microwave heating in terms of time and energy losses.

The input parameters of such measurements are the oil mass m, the microwave output power P and the heating time t. The output variable is the temperature of the oil T. The microwave maximum output power was $P = 950W$ and we considered the value written on the oven display as a realistic indication of the radiation power present in the oven cavity during the operation, averaged over time (see section 2.2.1). The heating time was set on the oven controller (with a resolution of 1s) and the oil mass was measured with an electronic scale with a resolution of 0.01g. The containers for the oil were a glass beaker and a plastic bucket. The first was used for masses up to 700g, while the latter was used for higher masses, up to 2kg. Repeated experiments showed that different sizes and materials of the container did not alter the heat transfer to the oil, within measurements error.

After the heating process, the oil was quickly stirred with a glass stick to avoid big temperature in-homogeneity. The temperature was measured with a PT100 thermocouple with a resolution of 0.1° C and such measurement was performed within 10s after the heating process in order to reduces heat losses. Due to the residual in-homogeneity in temperature between different parts of the oil volume we considered the error on the temperature to be within 1° C.

Three series of measurements were performed by changing only one of the input parameters at a time. The chosen sample for the measurements is 2-ethylhexyl stearate.

2.4.1   Temperature vs Time

First we measured the final temperature reached by the microwave heated oil as a function of the heating time. We performed a series of measurements keeping constant the weight of the sample at $m = 600g$ and the power of the microwave at $P = 350W$. We acquired the final temperature of the sample at fixed time steps with the aforementioned method. As it can be seen in Figure 2.11, there is a linear relation between temperature and time. The linear fit, with null intercept,
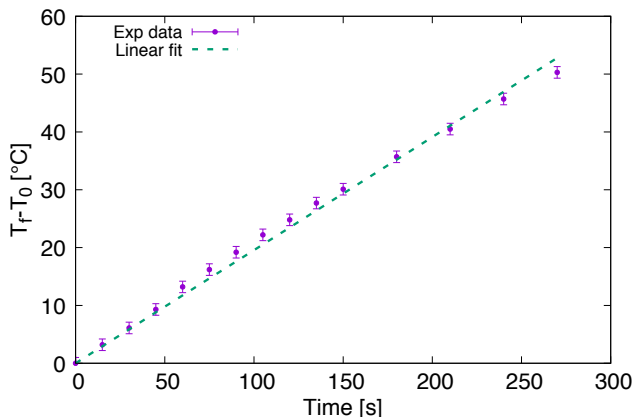
Figure 2.11: Temperature difference measured in the oil as function of time of heating, keeping constant the average microwave output power

is in the form:

$$\Delta T = \alpha \Delta t$$

with $\alpha = 0.19 \pm 0.01 K/s$. All the fit calculations reported in this section were performed using Gnuplot 5.2 [11]. Specific heat is related to the linear fit parameter α by:

$$c = \frac{P}{\alpha\, m}$$

We know that the specific heat for this kind of oil is around 2 ± 0.1 kJ kg^{-1} K^{-1} [1] but we were not able to extrapolate it from our data since we are not able to estimate the heat losses or the transfer of microwave energy to other parts of the setup.

2.4.2   Temperature vs Power

We took a second series of data to recover the relation between the final temperature of the sample and the output power of the microwave. We set a heating time of $t = 90s$ and a weight of the sample of 450g, then we varied the MW output power from 0 to 950W, which was the maximum power obtainable with our apparatus, and we took measurements of the final temperature for each power step (Figure 2.12). Analyzing the behavior of the data and fitting them with a linear
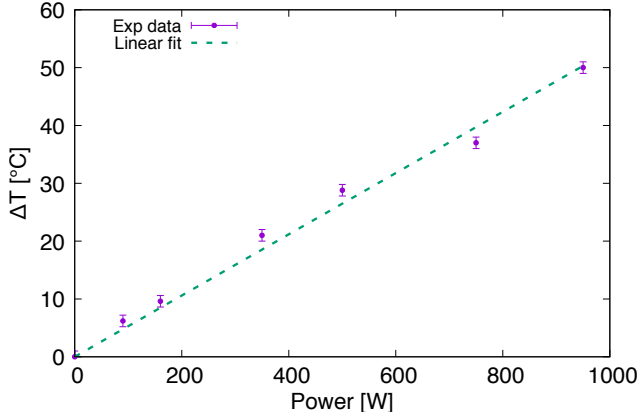
Figure 2.12: Temperature difference measured in the oil as function of the output power, keeping constant the oil mass

function we can observe also in this case a linear increase of the temperature of the sample as function of the power provided, with the relation:

$$\Delta T = \beta P$$

with $\beta = 0.053 \pm 0.002 \mathrm{K/W}$. We can again link this value to the specific heat of the system:

$$c = \frac{\Delta t}{\beta m}$$

2.4.3 Temperature vs Mass

The third set of measurements we performed was aimed to understand the relation between the mass of the sample and its temperature variation. We kept constant the heating time at $t = 90\mathrm{s}$ and, since we used two different values of MW output power ($500W$ for lower masses and $950W$ for higher masses), we normalized the variation of temperature for the energy provided by the microwave (Figure 2.13). We can observe an hyperbolic behavior of the collected data, with an inverse relation between the mass of the sample and its temperature variation in the form:

$$\frac{\Delta T}{E} = \frac{\gamma}{m^{1+x}} + \delta$$

with $\gamma = 0.21 \pm 0.02$ K kg/W. The terms $x = 0.14 \pm 0.06$ and $\delta = 0.10 \pm 0.02$ K/W provide corrections from the ideal hyperbolic behaviour of the thermodynamic equation

$$\frac{\Delta T}{E} = \frac{c}{m}$$

These corrections take into account the heat lost in the contact between the oil, the container and the air and the power transferred by the microwave to the other parts of the setup inside the cavity.
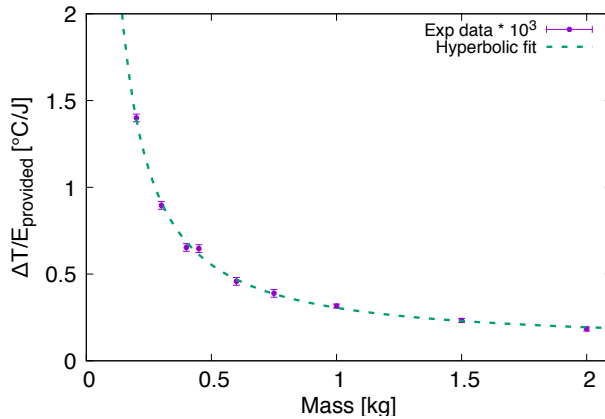
Figure 2.13: Temperature difference (normalized by the power output) measured in the oil as function of the oil mass
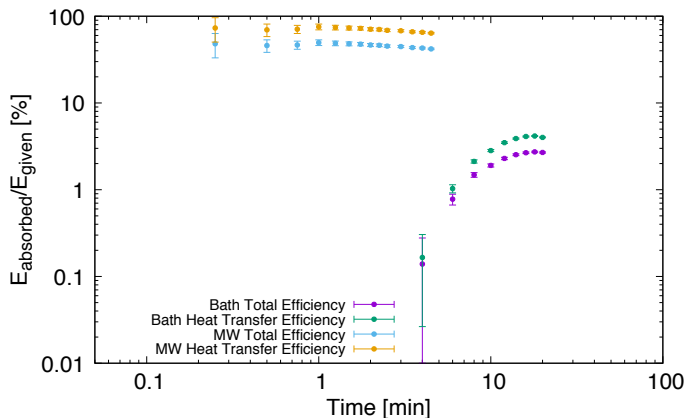
2.4.4   Efficiency

Figure 2.14: Efficiency comparison between thermal bath and microwave heating systems.

Finally, using the data acquired from the thermal bath regarding the behavior of the final temperature of the sample as a function of heating time, we compared the efficiency of the two methods for the oil heating: the thermal bath, already used by the company, and the MW. To obtain the total efficiency, we divided the energy transferred to the oil by the total energy absorbed by the set up (measured with a power meter attached to the electrical plug). The heat transfer efficiency was calculated, in the case of MW heating, by dividing the transferred energy by the energy of the MW field (indicated on the display). In the case of the thermal bath we calculated the heat transfer efficiency between the water and the oil by dividing the energy of the oil by the sum of the thermal energies of the oil and the water bath (that is the total energy in the bath which is available to heat the

oil). The results of the calculation are shown in Figure 2.14.

We can easily understand that the heating method using the MW is a several times more efficient than the thermal bath one with a total efficiency reaching 50% in the case of the MW and only 3% for the thermal bath. At the same time it can be seen that MW is also more efficient in terms of time: in fact, the oil in the MW oven starts heating up immediately while in the thermal bath the resistors must first heat the water and the steel casing and only after some minutes the oil starts to heat up.

2.5 Possible industrial implementation

During microwave heating, the electromagnetic energy provided by the microwave is transferred from the microwave's waveguide to only small volume regions of the heated sample. This process causes large temperature inhomogeneity inside the oil samples. From an industrial point of view, the knowledge of the exact positions of the hotspots inside the microwave heated oil is fundamental in order avoid oil degradation. In this section we will discuss about how it is possible to predict the location of such heat spikes by simulating the heating process induced by microwaves. The simulation we implemented shows what happens when the sample material is heated by an electromagnetic field of fixed power (900 W) and frequency (2.45 GHz) for some amount of time. During the heating time of the simulation, we monitored the temperature increase and, in general, the temperature pattern inside the material. Simulation is performed using a finite element software COMSOL-multiphysics 5.0. We want also to report that the same approch to simulate the microwave heating problem is used in [2]

2.5.1 Geometrical model

The design of the oven geometry is shown in Fig. 2.17 where dimensions are $39.5\,\text{cm} \times 37\,\text{cm} \times 21\,\text{cm}$. On the left side of Fig. 2.17 we observe the presence of double waveguides. The waveguide apertures are $9\,\text{cm} \times 2\,\text{cm}$ large. From these the electromagnetic energy from the magnetron is delivered inside the cavity. In the simulation, we assumed that the power input in the cavity by the two waveguides is exactly the same. We have used a symmetry cut to halve the model size so that we only input $225\,\text{W}$ per each waveguide. This symmetry consideration dramatically reduces the computational effort needed to perform the simulation without loss of information about the physical behavior of the system.

We set the walls of the oven and the waveguides to be made of copper material. Inside the oven, we place a sample disk, which is composed of 70% water and 30% palm oil. The disk has a radius of $13\,\text{cm}$ and it is $1\,\text{cm}$ thick. The dielectic costant ε is the physcal parameter which describe the power absorption in a medium. In the general case, the dielectric constant is a function of the frequency and temperature of the medium, $\varepsilon = \varepsilon(\nu, T)$. The complex notation $\varepsilon = \varepsilon_R + i\varepsilon_I$ allows also to assign different physical meanings to the real and the imaginary part of the dielectric constant. ε_R is related to the reflection and
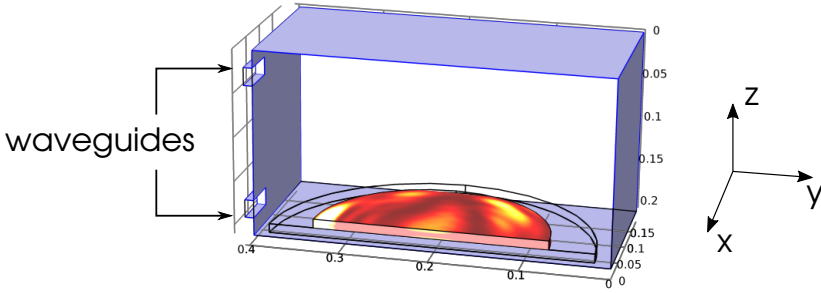
Figure 2.15: Oven geometry, where the red halved disk represents the sample material heated by the microwaves. The temperature map shows the hotter spots in clear color, while the colder spots in dark color.

the transmission of electromagnetic power through the medium. ε_I accounts for the absorption process during the energy transfer. In Tab. 2.1 we detail the real and the imaginary part of the dielectric constant of the materials involved in the COMSOL Model. We also report the effective dielectric constant used to set the sample disk parameters in the simulation (namely, cream).

material	ε_R	ε_I
H_2O	70	10
oil palm	3	0.3
cream	54	9.3

Table 2.1: Dielectric costant comparision. The dielectric costant values are taken in the microwave regime. Oil palm values can be found in [12]. The cream is suppose to be a compound of water (70%) and oil (30%). All the values reported in the table are units of vacuum dielectric costant $\varepsilon_0 = 8.85 \times 10^{-12}\,\mathrm{F/m}$

When the oven is switched on, the cream starts to absorb some of the power input in the cavity and the cream temperature starts to increase. The energy transfer process has been simulated for a period of 30 s. In this interval, we assumed that the dielectric constants are independent of the temperature of the material.

2.5.2   Temperature distribution as a function of time

For our purpose, we were interested into monitoring both the highest temperature peak and the temperature pattern throughout the disk. Fig. 2.16 shows these data for different heating times. In the upper panels, we can see the temperature profile along the disk, while in the lower panel we report the highest temperature value reached at each time step. As we can see, the temperature increases linearly during the heating simulation. After 30 s the hottest hotspot is almost at 400 °C.
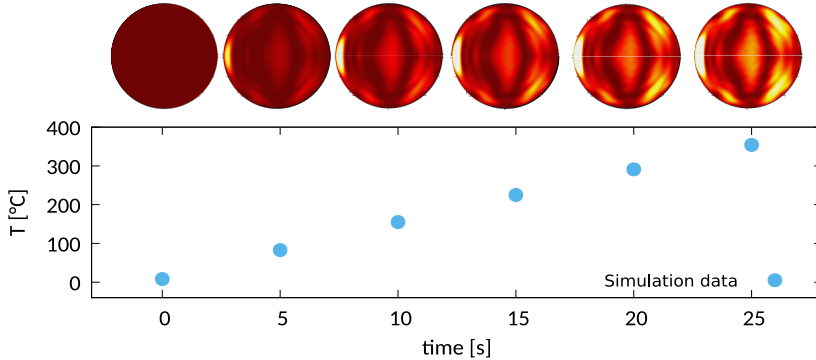
Figure 2.16: Heat pattern as a function of time. Above the plot is possible to observe how the temperature patter change in time. The plot reports the highest temperature achived inside the cream as a function of heated time.

By comparing these results with the experimental data recorded with a real MW oven we can claim that:

- the data obtained in our simulation are in good agreement with those obtained with an infrared camera and with a thermocouple during the experiments;

- the temperature pattern is not symmetric in the xy-plane: the highest temperature is reached nearby the waveguides, where the MW source is located;

- the hotspots are clearly visible by naked eyes, which means that the temperature is high enough to ruin the water / oil palm emulsion. The degradation of the emulsion caused by temperature is an important parameter to monitor from an industrial point of view.

2.5.3 Temperature distribution as a function of the position

In this paragraph, we focus on the temperature distribution inside the cavity during the oven operation. In order to compare the experimental results with the simulations, we built a multi-layered structure with each filled by wax. Fig. 2.17(a) shows the multi-layer stack as it has been prepared for the physical test. In Fig. 2.17 (b) we report the simulation output, in which four disks have been heated by MWs. We stress that the plastic structure used to hold the wax disks in the right position inside the oven are not heated by the MWs. For this reason, only the wax material competes to the heating. Fig. 2.16 reports the temperature pattern observed after 30 s of MW heating. In the upper panels, we have four pictures obtained with a FLIR thermo-camera placed above the real layers after the MW heating.

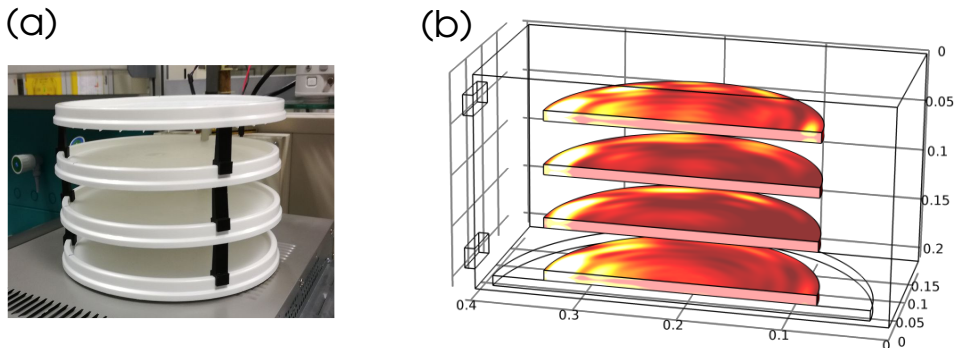Relying on these qualitative results, we can provide the following considerations:

(a)

(b)

Figure 2.17: **(a)** "Real" multi-layered structure with plastic skeleton and plastic dishes filled with the wax. **(b)** Simulation of the multi-layer in a halved oven geometry during operation.

- the maximum temperature achieved in this experiment is almost a quarter of the maximum temperature reached in Fig (2.16). This means that the temperature reached with MW heating is directly related to the amount of material to be heated;

- the positions of the hotspots are correctly predicted by the simulation;

- the symmetry pattern along the z-coordinate, due to the waveguides positioning (one above the other) is clear in the simulation but is less evident from the infrared images: this outcome could be explained with a non-equal power splitting between the waveguides;

- from the infrared images, we can observe that the maximum temperature value is reached in the bottom wax layer: this suggests that more power is ejected from the bottom waveguide in the oven used to perform the experiments.

2.6   Conclusions

During the IPSP week we tackled the problem proposed by Areaderma, i.e. the feasibility of MW oil heating for industrial purposes, following the workflow presented in Fig. 2.1. In particular, we probed the chemical properties of heated oil, and provided a numerical approach to predict the presence and the positions of hotspots within the oil sample. All the considerations and discussions reported in the previous pages can be finally summarised in the schematic reported in Fig. 2.19. We understood that MW oil heating is possible and that the physics behind the heating process is the same behind the MW heating of water, i.e. dieletric heating. However, this technique does not provide a homogeneously distributed
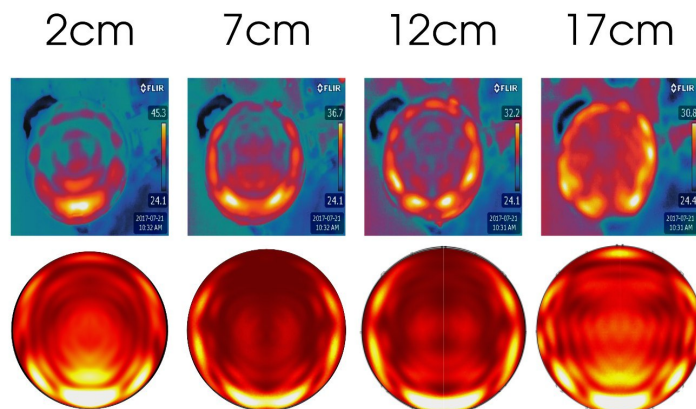
Figure 2.18: Comparison among the simulated layers and the experimental ones. The pattern of each layers is compared at each different z-position. On the top of the figure, the experimental layers are taken using an infrared camera. On the bottom of the figure, the simulated layers are shown.
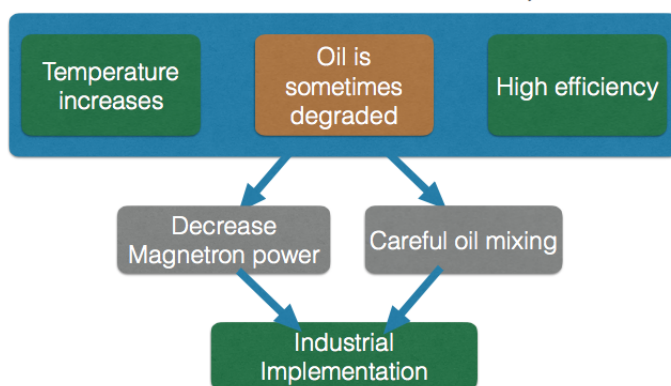

Figure 2.19: Schematic representation of the caveats one needs to take into account for the industrial implementation of the microwave heating process

temperature profile within the sample: in fact, during the heating process, localised regions, hotspots, can reach very high temperatures compared to the rest of the sample. In the case of single-molecule oils like 2-ethylexyl stearate, hotspots do not represent a problem, since its chemical properties are not affected by the measured high temperature peaks. Multi-component oils, however, might be less robust to such high-temperature exposure, due to the volatile and thermolabile parts in their compositions. Thus, caution should be employed, and chemical analyses should be performed for every oil used in the industrial process. Our studies also showed a dramatic gain in efficiency of the MW heating with respect

to the oil resistive heating, which is currently employed in the Areaderma facility. Although there is an evident improvement in changing the heating process, two main caveats should orient the industrial implementation of the MW radiation:

- the magnetron power should be designed in order to provide a temperature consistent with the chemical properties of the oils;

- a thorough mixing of the oil has to be implemented, since the temperature profile is not homogeneous and the rotating plate, currently used in consumer products, does not guarantee an efficient distribution of heat.

In order to do so, we showed that optical simulations can be used as a guide for the industrial implementation, being those able to predict, with reasonable accuracy, the positions of the hotspots and their respective temperature. Finally, we would like to highlight that the presence of the hottest hotspots, which are located, in the outer portion of the sample might be modulated by employing a modified version of the proposed process. The heating device could, in fact, include a water jacket around the oil bucket, and the resonance cavity could be designed in order to form hotspots in this outer jacket. In this way, the oil would be heated both by the heat transmission from the surrounding water, and by the microwaves, in a *hybrid* water-MW heating process. This solution could avoid the possible oil degradation in these regions. Due to the limited amount of time, this strategy was not further investigated, but can still provide a useful hint for the future industrial route.

Bibliography

[1] Private communications with Areaderma's spokesman.

[2] Michael Vollmer, *Physics of the microwave oven,*Physics Education **39** 1 pag.74 (2004)

[3] William Humphrey and Andrew Dalke and Klaus Schulten, *VMD – Visual Molecular Dynamics*, Journal of Molecular Graphics **14**, 1996

[4] `https://pubchem.ncbi.nlm.nih.gov/compound/2-Ethylhexyl_stearate#section=3D-Status`

[5] James C. Phillips, Rosemary Braun, Wei Wang, James Gumbart, Emad Tajkhorshid, Elizabeth Villa, Christophe Chipot, Robert D. Skeel, Laxmikant Kale, and Klaus Schulten, *Scalable molecular dynamics with NAMD*, Journal of Computational Chemistry **26**, 2005

[6] Klauda, J.B., Venable, R.M., Freites, J.A., O'Connor, J.W., Tobias, D.J., Mondragon-Ramirez, C., Vorobyov, I., MacKerell, Jr., A.D., and Pastor, R.W., *Update of the CHARMM All-Atom Additive Force Field for Lipids: Validation on Six Lipid Types*, Journal of Physical Chemistry B **114**, 2010

[7] E.M. Mahmoud et al., *Oxidation of olive oils during microwave and conventional heating for fast food preparation*, Czech J. Food Sci. **27**, S173 (2009)

[8] H. Yang, J. Irudayaraj, M.M. Paradkar, *Discriminant analysis of edible oils and fats by FTIR, FT-NIR and FT-Raman spectroscopy*, Food Chemistry **93**, 25 (2005)

[9] S.T. Forrester, L. Janik, *Total Petroleum Hydrocarbon Concentration Prediction in Soils Using Diffuse Reflectance Infrared Spectroscopy* Soil Science Society of America Journal **93**, 450 (2013)

[10] S.T. Forrester, L. Janik, *Visible Raman spectroscopy for the discrimination of olive oils from different vegetable oils and the detection of adulteration* Journal of Raman Spectroscopy **40**, 1284 (2009)

[11] Williams, T. and Kelley, C. (2011). Gnuplot 4.5: an interactive plotting program. URL `http://gnuplot.info`.

[12] A.S. Arshad et al., *Dielectric properties and microwave heating of oil palm biomass and biochar*,Industrial Crops and Products **50** 366 - 374 (2013)

[13] Santos et al., *3D electromagnetic field simulation in microwave ovens: a tool to control thermal runaway*,COMSOL Conference (2010)

[14] Vollmer M., *Physics of the microwave oven*, Phys. Educ. **39**, 2004

THREE

FILM-BASED DOSIMETRY OF IONIZING RADIATION

M. Caffini, D. E. Chiari, M. Finazzer, E. Macaluso, N. Pagno, A. Perinelli, D. Proverbio, L. P. Rignanese, M. Zanoli, M. Zanon

3.1 Introduction

3.1.1 The company

Tecnorad [1] was founded in 1976 by Renato Milanesi, physicist and radiation protection expert. The main goal of the company is to provide a high quality dosimetric measurement to the customers. From 2009 Tecnorad took part every year to the EURADOS (European Radiation Dosimetry Group) meeting [2], passing the tests for all the different kinds of dosimetric methodology: film badge dosimetry, ring and bracelet TLD, and fingertip TLD for Beta radiations. As proved by these achievements and by its certified standard ISO 9001:2015, Tecnorad is among the first companies at European level and an Italian excellence in the field of dosimetry.

3.1.2 Film dosimetry

Some of the early scientists working with what turned out to be radioactive elements discovered radioactivity because photographic films had been stored near to radioactive material and images were impressed on the films by the emitted radiation. The film dosimeter device was developed by Ernest O. Wollan in 1948 [3]. Nowadays the film badge dosimeter is used to measure and record radiation exposure due to Gamma rays, X-rays and Beta particles. The badge dosimeter consists in a PVC holder where the photographic film is hosted. More in detail, the holder consists in two plastic parts on which metal filters (of copper and lead) are stuck; the films are enclosed in the inner part. The filters have standardized dimensions as reported in Figure 3.1.
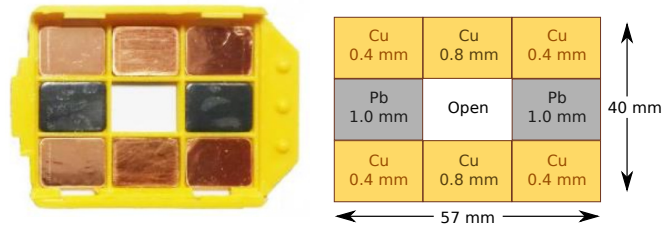
Figure 3.1: Plastic badge with metal filters.

When the film is irradiated, an image of the metal filters is projected on the film. Depending on their energy, photons are attenuated preferentially by different absorber materials. This property is exploited in film dosimetry to identify the energy of the radiation to which the dosimeter was exposed: knowing the energy of the photons allows for an accurate measurement of the radiation dose. The absorbed dose is measured in Gray (Gy) which quantifies the absorbed energy per unit mass (1 Gy = 1 J·kg^{-1}).

Each filter has a different penetration length of the ionizing particles, leading to a different blackening degree in the film (Figure 3.2). The ratio between these blackening values allows to compute the energy of the incident radiation and therefore the dose. The films can be used for measurements of incident photon energy in the range between 15 keV to 6 MeV and of *equivalent* doses between 0.01 mSv and 2 Sv. The Sievert (Sv) is a derived unit for the ionizing radiation equivalent dose: it is proportional to the physical quantity of absorbed energy per unit mass (measured in Gy), but also takes into account the biological effectiveness of the radiation with a coefficient depending on the kind of impinging radiation and, in some cases, on the tissue that is being exposed.

Film dosimetry is provided by Tecnorad as a periodic subscription, with the customers receiving their personal dosimeter to be worn as a badge. Once used, the dosimeters are shipped back to Tecnorad where they are analyzed and the radiation dose is measured. Actually, each dosimeter contains two films produced with different emulsions of different sensitivity, one for low doses (high sensitivity) and the other one for high doses (low sensitivity) measurements: when the low-dose film is saturated (completely black), the second film is considered. After use, the films are removed from its PVC holder (protecting it from light exposure and water) and developed in order to measure exposure.

What can be measured directly is the optical density of the film exposed to the radiation. Once the optical density for the different regions under the metal filters (i.e., for different energy sensitivities) are known, the equivalent dose is computed by means of a nonlinear multiparametric fitting that gives the most probable energy and dose value. The kind of exposure (diffuse, direct, from different angles, etc.) can be inferred from the pattern drawn by the filters on the film itself: Figure 3.2 shows different patterns that can be produced by different types of exposure.
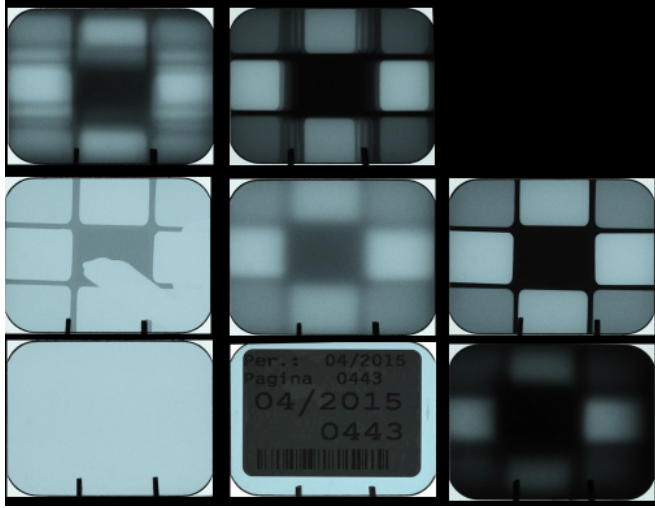
Figure 3.2: Typical appearance of film dosimeters. An unexposed film is shown in the bottom left corner; a completely saturated one is shown in the top right corner. The central film of the bottom row is a "control film" used typically at the beginning of a series to identify it. The other films show different levels of exposure, both in intensity and in direction.

Figure 3.3: Example of calibration strip with 17 regions of known optical density.

3.1.3 Optical density

Optical density, often referred to as "absorbance", is the base-10 logarithm of the ratio of incident to transmitted radiant power through a material [4], i.e.

$$\mathrm{OD} = \log\left(\frac{I_0}{I_t}\right) \tag{3.1}$$

where I_0 is the intensity of the incident light on the film and I_t the intensity of the transmitted light. Sometimes, the natural logarithm is taken instead, and the resulting quantity is called "optical depth". Reference optical densities are provided by calibrated film strips, consisting of about twenty different zones of known optical densities (see Figure 3.3 as an example). These strips are used to calibrate instruments. The typical optical density range of interest is from 0.2 to 5 or 6 OD, corresponding roughly to an attenuation from a factor $1/2$ up to 10^{-6}.

The instrument used in the industry to measure the optical density of a small region of the film is the optical photodensitometer (Figure 3.4). However, this instrument has to be operated manually, with a consequently high time cost and with a human error contribution to the uncertainty of the measurement. Moreover, this kind of device is not produced anymore: the company cannot rely on this method any longer and aims at the development of a new, automatized system.

Figure 3.4: Portable manual photodensitometer. These devices are not produced anymore.

3.2   The problem

The optical density measurement with a photodensitometer is slow and prone to multiple errors due to the needful human interaction with the instrument. The automation of this measure is necessary to the company to compete on the dosimetry measurement market. Tecnorad tried to solve this problem building the HORUS machine (shown in Fig. 3.5). During the 2017 IPSP edition, the company allowed the team to physically examine this machine in order to understand the difficulties related to this automation process and try to solve the problems afflicting it. HORUS is made of four main components:

Storage system A rotating cylindrical wheel containing multiple baskets which contain up to 48 exposed film each.

Positioning system Two small tweezers that take the films one by one and put them in between the light source and the camera.

Light source A commercial, low-end LED panel.

Acquisition system A very high-resolution (up to 40 Mega Pixels) medium format Hasselblad HD40 camera, coupled with a 120 mm macro lens.

Beside the automation process, the task of the HORUS machine is also the identification and classification of the direction of the radiation that impressed the dosimetry film (see Section 3.1, Fig. 3.2). Sadly, HORUS does not permit a good estimation of the OD but it is useful for the classification. During the 2017 IPSP edition, the team inspected the machine finding problems that degrade the quality and the resolution of the OD measurement. It was immediately clear that the main problem was the positioning of the film with respect to the light source and the camera. The tweezers take the film from the storage basket placing it in front of the LED panel at a distance of $\sim 20\,\mathrm{mm}$. This gap, in addition to a poor "shielding" from the environment, allows a lot of light to diffuse inside the measurement chamber and to reach the camera, thus corrupting the OD measurement. The camera detects both the light passing through the film (I_{OD}) and the diffused light (I_{DL}): what is measured, then, is $I = I_{OD} + I_{DL}$. The

Figure 3.5: The HORUS machine. The rotating wheel is visible at the back of the device.

I_{DL} contribution consists of a variable background which is very hard to estimate, thus resulting in a lower dynamic range of the camera and a poorer resolution in the OD measurement. By putting the calibration film in contact with the LED panel, isolating it from the surrounding light, and taking a photograph with the original camera acquisition system it was possible to distinguish up to OD 3 (see Fig. 3.6).

After the investigation on the light source, it was clear that the HORUS LED panel could not provide the high performances required for the OD measurement. The panel had poor spatial homogeneity, poor output power and showed a "blue-shifted" spectrum. The very high-resolution camera cannot resolve an OD higher than 3 in a single shoot. As a possible solution, the dynamic range could be extended by taking more photos of the same film with different exposure setting, and then make a clever merging of them. The merging software process is called High Dynamic Range (HDR) [5] and, after an accurate calibration process, allowed to improve slightly the OD measure. However, the process is time consuming and resource greedy.

The HORUS software that performs the film classification is not optimized for the task. In fact, it is built on a general-purpose machine learning kernel, which is too complex for the task of classifying dosimetry films and suffers from overfitting issues, besides being too computationally expensive.

From all these considerations, the team developed the following line of action. Part of the team worked on designing and testing a prototype device that could measure optical densities with good accuracy up to OD $\simeq$ 6; this experimental
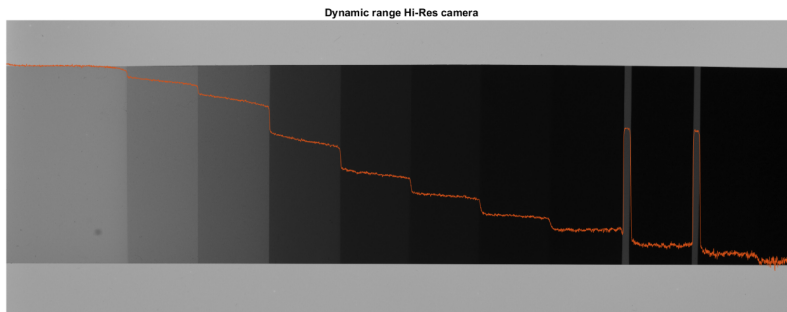
Figure 3.6: Calibration strip as acquired by the camera once a better isolation was provided. The red line, corresponding to the by-column average of the pixels intensity, highlights the camera capability in detecting different shades of gray, i.e. different levels of optical density. The last piece of the strip corresponds to OD = 3.04.

study is the subject of Section 3.3. The developed prototype was designed from the very beginning with the aim of making it fully automatic, according to the company needs. On the other hand, the rest of the team worked on the classification software, building a new algorithm from scratches: Section 3.4 describes this development. The software is not only aimed at classification, but also at providing instructions – to the "hardware part" – about which regions of the film should be measured. The purpose of this cooperative approach was to design a device that could first take a photograph, classify the film, choose whether the film is worth measuring with the dedicated apparatus, and then – if it is the case – perform the physical measure. This integrated workflow is discussed in detail in Section 3.5, where a time-efficiency study is also presented.

3.3   Experimental study

The experimental investigation focused on providing a *proof of concept* for the feasibility of the optical density measure under conditions that are analogous to those existing in a future automatic device. Different kinds of experimental set-up and devices were studied in order to find the most suitable ones. The fundamental arrangement consists in a light source and a detector, with a reference film of known optical density put in between. A white, diffusive panel was put between the source and the film to obtain a more homogeneous illumination of the latter; this proved to be necessary in order to accomplish repeatable measurements.

Different geometrical arrangements for the source and detector were tested. The distance between source and detector was chosen to be the smallest possible ($\simeq 2\,\text{mm}$) to reduce the acceptance of environmental noise. In addition, the detector was collimated with a $2\,\text{mm}$ pinhole for the same reason. A scheme of the configuration that was found to best suit the requirements is shown in Fig. 3.7.
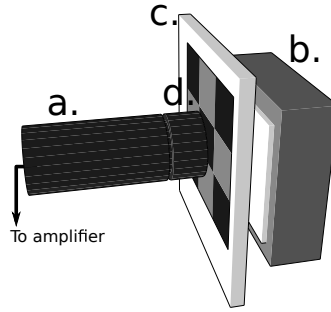
Figure 3.7: Schematic drawing (not to scale) of the apparatus for testing the sources, detectors and configurations. The source shown here is the LED matrix, discussed in the dedicated paragraph. a. Detector; b. Light source; c. Diffusive panel; d. Film.

Detector To choose a detector, both a power meter and a photodiode were tested. The power meter has the disadvantage of being a linear device, i.e. the output is exponentially dependent on the OD; moreover, the used power meter can reach a narrower range of OD compared to the photodiode. The best detector for the purpose is a photodiode used in photo-voltaic mode, that is, without any external bias. Since in this configuration the relation between the light intensity and the output voltage is logarithmic [6], in the photo-voltaic mode the measured voltage at the output of the photodiode is linearly dependent on the optical density. This is the best solution to achieve the wide range of OD (6 orders of magnitude) required.

In addition, the photo-voltaic mode has a better signal-to-noise ratio with respect to the photo-conductive mode [6], resulting in a more accurate measurement, especially at high optical densities. Therefore, a photodiode - without any external bias - is the optimal choice for the detector. The photodiode was connected directly to a preamplifier which output voltage was in turn read using a digital multimeter. The components used for testing are:

Photodiode Thorlabs CXA2590 mounted Si photodiode, SM05PD1A [7]

Preamplifier Stanford Research System SR560 low-noise voltage amplifier [8]

Multimeter Agilent 34410A 5 1/2 digital multimeter [9]

Source The main goal is to have a source with a sufficiently high luminosity so that a detectable signal is present also when the optical density is above 5. In addition, the source was studied taking in to account the emission spectra and the possibility to illuminate a small spot of the film, in order to avoid that the spurious scattering of light within a region not under measurement contributes to the observed intensity. The following sources were tested; the values of output voltage vs. the optical density of the reference film are plotted in Fig. 3.8. The power supply used for all sources was an Agilent 3631A DC Power Supply [10].

Lasers A small laser (two different wavelengths were tested) has enough power

for the purpose, but it is too focused, which results in the measurement being strongly dependent on the position of the film.

LED panel An LED panel (similar to that of the HORUS machine) can be used to perform the measure in terms of OD, but the projection on the film has a large spatial inhomogeneity. The inhomogeneity persists even with a diffusive panel.

LED matrix A matrix of power LEDs has proved to be the best solution, due to the fact that it can be used to illuminate the film with a diffusive panel. It has the power to reach high OD ranges, and a better homogeneity.

Apart from the geometric considerations done so far, the graph of Fig. 3.8 shows also that the LED matrix source performs best over all the range of optical densities. In fact, its behavior is closer to a linear dependence compared to the other sources. This can be ascribed to the higher overall radiant power emitted by the LED matrix: in this context, a higher input power provides a higher signal-to-noise ratio. The adjustable power-supply allowed to test different levels of light intensity.
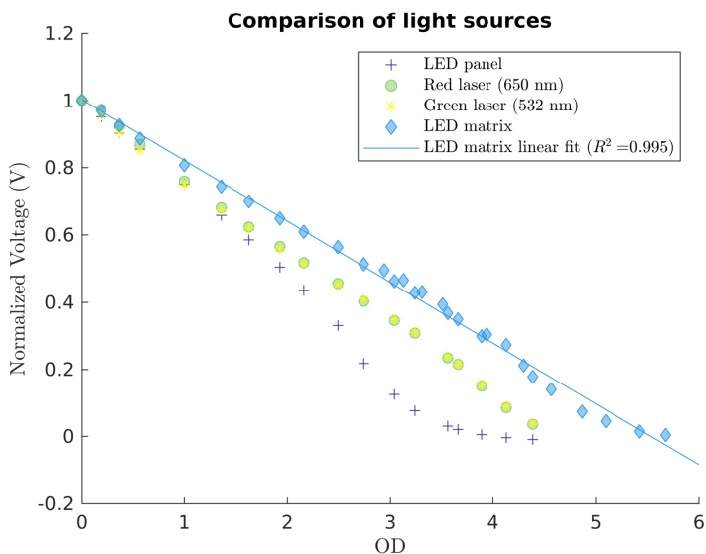
Figure 3.8: Experimental normalized output voltage of the diode versus OD for different light sources.

The performed measures have shown the ability of the apparatus to reach high optical density measurements with sufficient accuracy: performances better than those of the manual photodensitometer were proved. The geometry of the manual photodensitometer is correct for the task, but by using an improved source (both in terms of overall power and geometry) a more compact instrument could be designed, without the constraint of the isolation of the film from the

environmental light. Indeed, using the LED matrix and a distance of 2 mm it was possible to detect the signal discriminating it from external light with an OD of the interposed film up to 6. A wise choice of the detector working regime and a suitable readout electronics allowed to provide a relatively simple design that can be implemented in an automatic device: in section 3.5 this proposal is discussed, joining the experimental results of this section and the ideas for film classification of section 3.4.

3.4 Film classification

The original Tecnorad software was designed exclusively to classify film dosimeters. To this purpose, the company developed a software which core was a ready-made machine learning algorithm, very powerful for the discrimination of complex images but not optimized for the present task. The dosimeter images are fairly simple and, for this reason, the classification algorithm had overfitting problems.

Before discussing in detail the software developed by the team, it is worthwhile to clarify its aim. In fact, it does not have the purpose to fully characterize the film images, as the HORUS machine software has, but instead it should simplify and make as fast as possible the film analysis. So, once the Company requests is considered, together with the fact that most of the films (95%) come unexposed, the team decided to write a software able, first of all, to recognize this kind of films from the saturated ones and the clearly-impressed ones. Indeed, while for the formers none further measurement is required, for saturated films (< 1%) the corresponding low-sensitivity counterparts (see Section 3.1) must be considered; for the remaining films, several optical density measurements must be performed. Moreover, a way to find the most suitable regions where to measure the optical density was developed, in order to further improve the measurement accuracy. The most important characteristic of the developed software is the capability to cooperate with the "hardware" part in the perspective of a final, integrated device. Dosimeter pictures are acquired via a camera, then the software analyzes the images to check whether the film needs a detailed analysis, and if that is the case, finds the best regions to perform the measurement. Finally, the information is delivered to the hardware that can evaluate the optical density.

The core idea underlying the whole software is that the most relevant film features can be grasped by considering 6 stripe regions - 3 vertical and 3 horizontal, 10 pixels wide - crossing the 9 filters (see Fig. 3.9). From each of them, in order to reduce noise effects, a single intensity profile is obtained as the result of the average of the 10 profiles extracted from each 1-pixel wide stripe.

Unexposed and saturated films   Films which were not exposed to radiation and those completely saturated represent the easiest to recognize. As shown in panels (a) and (b) of Fig. 3.10, they are characterized by an almost uniform level of gray (corresponding to a given OD). In terms of the intensity profiles this feature, which uniquely describes unexposed and saturated films, leads to an
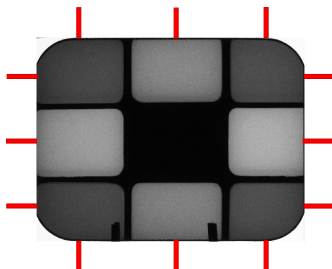
Figure 3.9: Typical image of a clearly-impressed film, in which the 9 different filter regions are distinguishable. Red lines indicate the considered stripe regions crossing the 9 filters, 10 pixels wide.

essentially flat curve (see Fig. 3.10(c)). At the same time, the two different kinds of films sharing this property are distinguished for the very different mean value of the intensity profiles. For the unexposed films, this value is higher than 0.5 (in relative units) while for the saturated ones it is typically lower than 0.1. In these cases, a most suitable region to acquire the optical density does not exist, but a single measure in the middle of the film is sufficient.
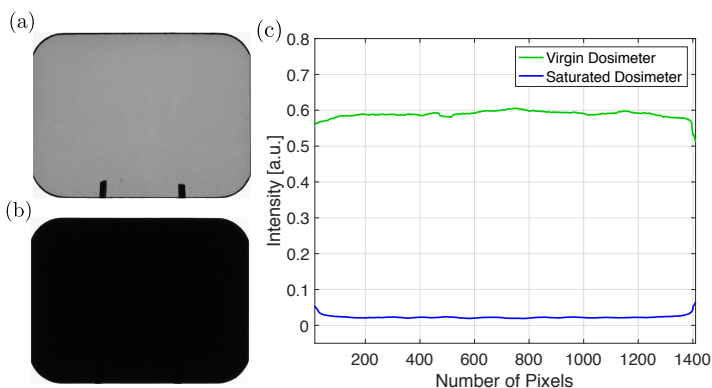
Figure 3.10: An unexposed film image (a), a saturated film image (b) and the associated intensity profiles (c).

Normally exposed films   In this case, all the dosimeter filters are impressed, even if in different ways, so it is necessary to acquire 9 values of optical density, one for each filter. In Fig. 3.11(a) the intensity profile obtained from the first column of the film is shown: the profile clearly identifies 3 separated regions and by analyzing the gradient of the profile itself (Fig. 3.11(b)) it is possible to divide in segments the film and define the most homogeneous region for each of the filters (Fig. 3.11(c)). For the sake of simplicity, the best suitable positions to acquire the OD measure is identified with the centers of these regions.
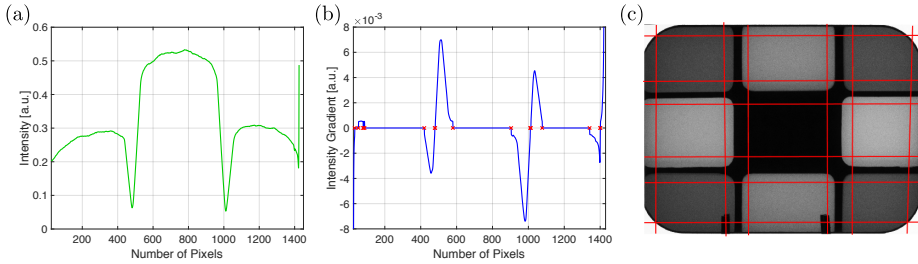
Figure 3.11: Intensity profile of the first column of the film, analyzed via a 10-pixels wide stripe (a), and its gradient (b). The film "segmentation" resulted from the analysis of the intensity profiles is shown in (c).
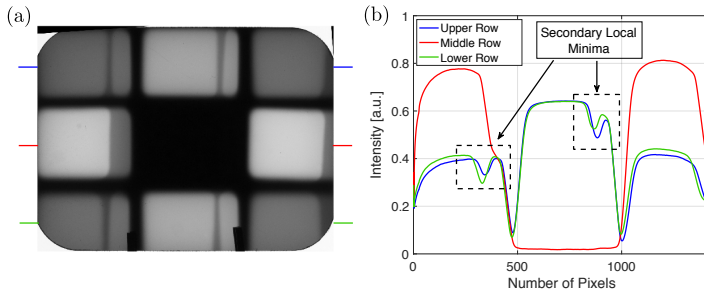

Figure 3.12: Doubtful classification case: a multiple exposed dosimeter is shown in (a). The presence of repeated filter edges is the main characteristic of this class of films. This evidence is shown by the occurence of secondary local minima in the intensity profiles (b).

Further developments   By establishing the regions of the film to be measured in terms of optical density, the proposed software accomplishes Tecnorad requirements to improve the measure both in terms of reproducibility and reliability. Furthermore, the software can be further improved in order to be applied to in-depth film classification. The algorithms developed during the week are able to correctly distinguish only between unexposed, saturated and clearly-impressed films. A more accurate analysis of the features (intensity profiles, profile gradients, etc...) can give information about the film irradiation history (multiple expositions, extended or point-like radiation sources, irradiation direction, and so on). The extraction of this further information can be performed by taking into account the presence of extra peaks or minima (see Fig 3.12), shadows in the images through gradient analysis and further details. Finally, the software can be also enriched with the capability of reading an identification matrix (a QR-code, as well as a simple barcode). The company is interested in this feature because it would provide a trustworthy way to identify the films.

3.5   A proposed integrated solution

A prototype of a device capable of processing the films was proposed by the team. The design process was guided by the knowledge acquired for what concerns the experimental tests of optical density measurements together with the developed classification algorithm, pursuing the idea of a single device working continuously on the films fed as input. The next section deals with the feasibility analysis of the proposed device, in terms of time efficiency. Fig. 3.13 shows a preliminary rendering with the core components of the proposed prototype. The key aspects of the proposed design are the following.

- A static light source, similar to the one that was found to perform the best (see Section 3.3), is used. The source is covered with a diffusive white panel, and each film is put directly in contact with the panel. The source-film-detector distances, combined with a detector collimation, are the most relevant parameter for reducing environmental contamination and spurious diffusions.

- The films to be processed are held in a sliding container, similar to those used in the HORUS machine; as the container moves, step-by-step, it allows a new film to be pushed up and locked in front of the light source. The pushing mechanism is part of the same structure that holds the light source.

- A camera takes a picture of the film just after the latter is put in position. The picture is processed for classification, and for the determination of the best points where the detector should be placed for the optical density measurement. When the film is unreadable, the successive measuring step is skipped. As a result of a time-efficiency evaluation analysis, the best policy is to carry on with the next film when an unreadable one is found, instead of waiting for the operator to analyze it by hand (see Section 3.5.1 for further details on this policy).

- An arm with the photodetector; the arm is moved by a servo system capable of an accurate 2-D positioning of the arm itself. The detector is put in contact with the film by the system just before each data acquisition (i.e., on each region of the film). The detector is a cheap photodiode in photovoltaic mode, as discussed in Section 3.3; its output voltage is read by a dedicated circuitry that amplifies it and digitize it before sending it to a computer.

3.5.1   Feasibility Analysis

The workflow automatization that TECNORAD wishes to achieve is not only meant to gain measurements objectivity and repeatability along with an improved precision, but also to speed up the whole film reading process. Therefore, it was tested if and how the solution proposed by the team would help the company in this direction. The efficiency of the manual procedure was then compared
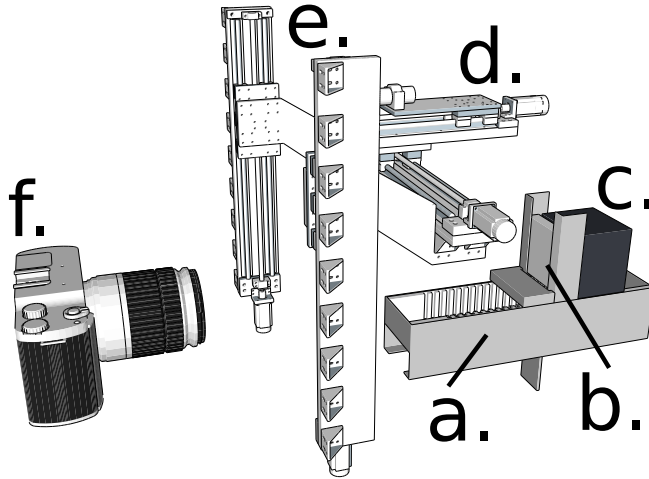
Figure 3.13: Rendering - with the only purpose of visualization - of the key components of the proposed device. a. Film holder, capable of sliding; b. Mechanism to place the film in measurement position; c. Light source with heat spreader; d. Detector for precise OD measurement; e. Servo system for detector positioning; f. Camera for pre-processing.

with the HORUS machine and with two proposed automatization solutions. The comparison parameter (referred to as *efficiency*) for a given method is quantified by the duty cycle

$$T = \frac{\text{Net time [min]}}{1000 \text{ processed films}};$$ (3.2)

efficiency is defined as $\eta = 1/T$. Within the "net time" are neither considered the film pre-processing nor the time needed to move films and workers around the facility, but only the actual processing time. Four solutions were compared: a human-only workflow, using manual densitometers, the HORUS machine, and the prototype proposed by the team either with human intervention whenever an unreadable film is found, or without it, in a continuous workflow: the doubtful cases would have been noted and, at the end of the whole process, a human operator could take them out and solve them. The latter procedure allows the machine to work even during night time, saving many working hours.

The films were divided into three classes, according to the everyday experience of TECNORAD experts: blank films, clearly-impressed films and doubtful films. The average population of films is made of 95% blank films, 4% clearly-impressed, and 1% doubtful films. This statistics was used to randomly generate films for the simulation. The time required for each film reading was estimated on the basis of the everyday experience of TECNORAD workers, on the hypothetic workflow or the proposed prototype, while it was measured directly for the HORUS machine. For human workers, random-duration delays (with 20 minutes mean and about 2-hours timing) were added to simulate pauses, and further small random delays were added to simulate distractions.

A proper script was written to simulate the behavior of a worker. Each sim-
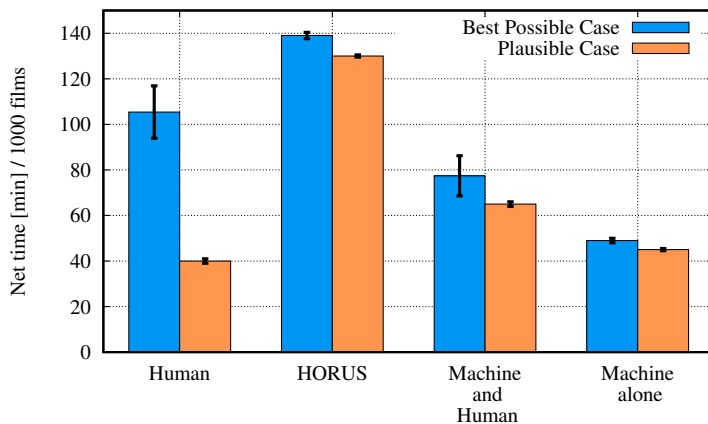
Figure 3.14: Results of the feasibility study simulation. Tecnorad experts confirmed that the simulated duty cycles for human workers are compatible with real ones.

ulated worker read an array of 1000 films that was previously randomly filled according to the distributions in the three classes: the total time that the simulation had taken each run was then used directly to compute efficiency. The script contains specific procedures that take into account systematic or stochastic delays and statistical variances. To provide a reasonable statistics, the whole simulation was run 200 times and results were averaged. Two sub-cases were considered: a "plausible" one (with delays, uncertainties etc.) and a "best possible" one (without uncertainties: everything works at its maximum speed). Finally, the results for each worker, along with their error bars, are shown in Figure 3.14. The histogram allows to draw some conclusions. As one would expect, the human worker efficiency is way more variable then that of machines. This can be seen both by comparing the plausible and the best possible case for the manual reading (leftmost columns), and by considering the absolute value of variances for the four procedures. The same variability is found when a machine is coupled with a human operator working in parallel (third pair of columns). This considerations justify, from an efficiency point of view, the desire of the company to automatize the whole process. However, as the histogram clearly shows, HORUS performances are worse than that of human workers for what concerns timing (although they are more repeatable). Any designed machine with a slight better per-film efficiency than that of HORUS can perform its job with a lower duty cycle; this can be achieved by applying some key improvements, for example by designing a completely different mechanical system, by reducing the photograph size and consequently the download time, by reducing the algorithm complexity, and so on. Having a human operator working in parallel with an automatic device is time wasting. On the contrary, if the machine discards by labeling the doubtful films and go on without stopping, its efficiency is close to the maximum and it can operate continuously. These reasons lead the team to design the machine following the fully-automatic paradigm described before.

3.6 Concluding remarks

Film dosimetry relies on the measurement of the degree of blackening of a photographic film, held inside a personal plastic badge, after exposure to ionizing radiation. Quantitatively, this is achieved by measuring the *optical density* of the developed film, an operation that requires high dynamic range in order to distinguish several orders of magnitude of transmitted light intensity through the film itself, down to OD 6, i.e. a transmitted intensity 10^{-6} times the incident one. Different regions of the films are covered by different metallic filters inside the badge, each one absorbing a different range of radiation energies: the impressed films thus contain also information on the kind of radiation and the exposure modality. Detecting and classifying these features provides a better insight on the radiation exposure suffered by the film user, therefore offering a more complete and useful service.

Tecnorad is a leading company in the field of film dosimetry. However, the present devices and procedures for both the optical density measurement and the film classification are severely lacking. First of all, OD measurements are performed with obsolete manual photodensitometers, that are slow and - due to the human factor - not very reliable. The attempt, by the company, to automatize the process via a high-resolution camera enclosed in an automatic machine has proved to be inadequate: indeed, the poor geometric arrangement of the components allows spurious light diffusion that limits the performances of the camera in discriminating high optical densities. In addition, the classification algorithm used by the machine is over-sized and not optimized for the task, yet computationally expensive.

During the IPSP2017 week the team tackled both the issues of providing an accurate OD measurement and of making it automatic, possibly with a single device capable of classifying the films and measuring the doses, without the need of human intervention. To improve the measurement process, the team worked on a source-film-detector hypothetical device with a wise choice of geometry and operational regimes, always aiming at a possible automatized and industrially efficient future machine. Different experimental tests were performed, and the best choice for the optical components and their arrangement was established. On the other hand, the team also worked to optimize the classification process, by re-writing the classification software and by changing its main task. The idea was not only to detect the already-mentioned features, but to decide what regions (if any) of the film are the ones worth measuring in terms of optical density.

The two research fronts were finally joined together in a single picture: the team proposed a preliminary design for a prototype of a device that accomplishes all the tasks required by the company. By integrating the first step of image processing - the "software" part - with the second step of optical density measurement - the "hardware" part - the proposed machine can provide a classification and a dose estimation with good accuracy, high reproducibility and, last but not least, an automatic, time-efficient workflow.

Bibliography

[1] http://www.tecnorad.it/

[2] http://www.eurados.org/

[3] L.A. Pardue, N. Goldstein, E.O. Wollan, *Photographic film as a pocket radiation dosimeter*, Atomic energy in biophysics, biology and medicine, 1948, **1**, 169

[4] R. Paschotta, article on "optical density" in the *Encyclopedia of Laser Physics and Technology*, https://www.rp-photonics.com/optical_density.html, accessed on 2017-10-24.

[5] S. Mann, R.W. Picard, *Being "undigital" with digital cameras: extending dynamic range by combining differently exposed pictures*, M.I.T. Media Lab Perceptual Computing Section, 1994, **323**, 422-428.

[6] B.E.A. Saleh, M.C. Teich, *Fundamentals of photonics*, 1991, New York, Wiley.

[7] Thorlabs, *Mounted silicon photodiode*, https://www.thorlabs.com/thorProduct.cfm?partNumber=SM05PD1A

[8] Stanford Research Systems, *Low-noise voltage amplifier*, http://www.thinksrs.com/products/SR560.htm

[9] Agilent, *Digital multimeter*, http://www.keysight.com/en/pd-692834-pn-34410A/digital-multimeter-6-digit-high-performance?cc=IT&lc=ita

[10] Agilent, *DC power supply*, http://www.keysight.com/en/pd-836433-pn-E3631A/80w-triple-output-power-supply-6v-5a-25v-1a?cc=IT&lc=ita

CREDITS

The Adige – BLM Group team

First picture
From left to right, first row: M. Zanoli, M. Previde Massara, S. Signorini, L. Parisi, C. Mordini.
Second row: A. Mezzadrelli, Y. Popat, M. Rossignoli.

Second picture
From left to right: M. Marcante, F. Getman.

© *Romano Magrone, University of Trento archive*
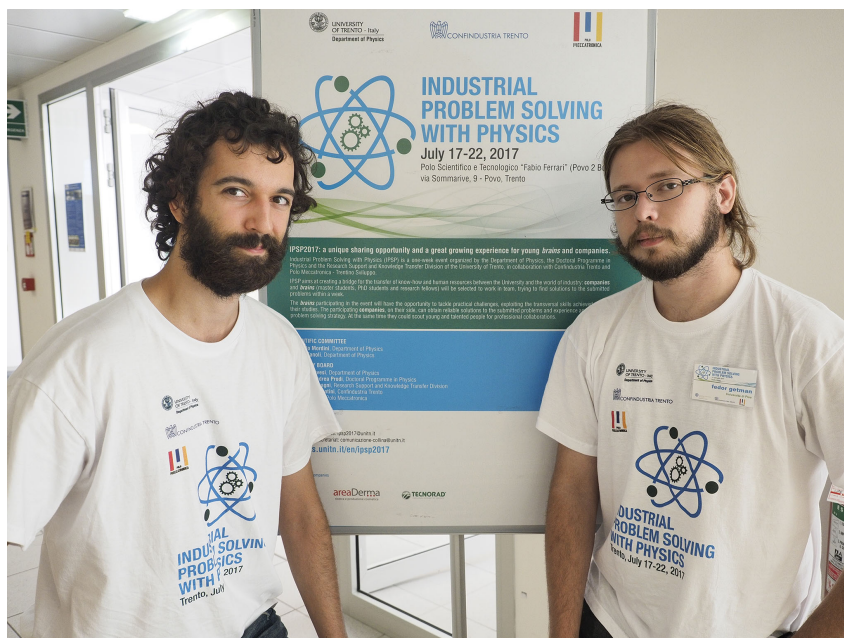
The Areaderma team

From left to right, first row: E. Andreatta, G. Prosdocimo, F. Bonaldo, P. Breviglieri, L. Basso, M. Stroppari, G. Abrusci, S. Merzi, L. Pavesi.
Second row: M. Zanoli, C. Mordini, T. Morelli, S. Malhotra, S. Orioli, M. Barbiero, L. Miori.

© *Romano Magrone, University of Trento archive*

The Tecnorad team

From left to right, first row: M. Finazzer, M. Caffini, D. E. Chiari, E. Macaluso, M. Zanon, A. Perinelli, N. Pagno, E. Braggio, L. P. Rignanese, R. Milanesi, D. Bonamini, L. Pavesi.
Second row: D. Proverbio, C. Mordini, M. Zanoli.

© *Romano Magrone, University of Trento archive*

ACKNOWLEDGMENTS

Looking back at 2014, when IPSP started, we think that with this edition we did not fail to meet the spirit which animated that first one. As Scientific Committee we did our best to fulfill our duties and to instill in all the companies we met the real take-home message of IPSP: that bridging together the young physics students and the industrial world is a key resource for transforming the challenges of today in the technology of the future.

In conclusion, we want to say «thank you» to the former Scientific Committees of IPSP and wish a successful work to the next one.

Industrial Problem Solving with Physics (IPSP) is a one-week event organized by the Department of Physics, the Doctoral Programme in Physics and the Research Support and Knowledge Transfer Division of the University of Trento, in collaboration with Confindustria Trento and Polo Meccatronica - Trentino Sviluppo. Its aim is to boost the connection between the world of the physics research and the world of industrial and applied technology.

3 companies and 30 brains (master students, PhD students and research fellows) are selected to work in team for a week, focused on finding innovative solutions to the industrial problems submitted by the companies.

The brains have the chance to tackle new practical challenges, making use of the knowledge and skills achieved during the course of their studies, while the companies experience alternative strategies towards the solution to their problems. These two ingredients prove again IPSP as a successful opportunity for building collaborations between young and talented people from the university and the world of industry.

SCIENTIFIC COMMITTEE

Carmelo Mordini, Department of Physics
Marco Zanoli, Department of Physics

ADVISORY BOARD

Lorenzo Pavesi, Department of Physics
Giovanni Andrea Prodi, Doctoral Programme in Physics
Vanessa Ravagni, Research Support and Knowledge Transfer Division
Alessandro Santini, Confindustria Trento
Paolo Gregori, Polo Meccatronica

events.unitn.it/en/ipsp2017

Participant companies

BLM GROUP
ADIGE

areaDerma
ricerca e produzione cosmetica

TECNORAD®
PERSONAL DOSIMETRY SERVICE

ART>UNITRENTO | March 2018